Computer Methods in Applied Mechanics and Engineering 418 (2024) 116462

Contents lists available at ScienceDirect

Computer Methods in Applied Mechanics and Engineering

journal homepage: www.elsevier.com/locate/cma

# A semi-implicit material point method for coupled thermo-hydro-mechanical simulation of saturated porous media in large deformation

Jidu Yu [a], Jidong Zhao [a,*], Weijian Liang [b], Shiwei Zhao [a]

[a] Department of Civil and Environmental Engineering, Hong Kong University of Science and Technology, Clearwater Bay, Kowloon, Hong Kong, China

[b] Department of Civil and Environmental engineering, Hong Kong Polytechnic University, Kowloon, Hong Kong, China

ARTICLE INFO

*Keywords:*
Thermo-hydro-mechanical coupling
Material point method
Granular media
Large deformation
Fractional step method

ABSTRACT

The coupled thermo-hydro-mechanical (THM) response of liquid-infiltrated porous media underpins the safe operation and maintenance of key engineering infrastructure. Challenges remain in modeling and understanding the complicated multiphysics processes of porous media subjected to THM loads and undergoing large deformation. In this study, we develop a stabilized material point method (MPM) for modeling the THM responses of large deformation problems in biphasic solid–fluid mixtures. A novel and efficient staggered solution scheme is proposed to solve the governing equations of the coupled system formulated in terms of four primary variables: solid displacement ($\boldsymbol{u}$), liquid velocity ($\boldsymbol{v}$), pore pressure ($p$), and temperature ($T$). The scheme solves the energy balance equation first and employs the resulting temperature to further advance the calculation of the momentum and mass balance equations using a semi-implicit fractional step method to facilitate equal-order interpolations. Both the incompressible and weakly compressible fluid are considered in the presented fractional step formulations. We also develop the axisymmetric form of the coupled MPM to increase the applicability and efficiency of the method in THM problems. The validity, stability, and robustness of the proposed method are demonstrated through three benchmark problems, including the heating of a saturated half-space, the non-isothermal consolidation of a soil column, and a three-dimensional axisymmetric problem pertaining to the thermoelastic response around a point heat source. The predictive capability of the proposed method for large deformation problems is further showcased by the simulation of the progressive failure process of a thermal-sensitive slope.

## 1. Introduction

Climate change and energy crisis pose challenges to the design and operation of key infrastructure in civil engineering in tackling complicated coupled thermo-hydro-mechanical (THM) conditions. Pertaining examples in geotechnical engineering are the geothermal pile foundations [1], the marine gas hydrate exploitation [2], the radioactive waste disposal [3], and the geothermal reservoirs recovery [4]. Natural geohazards, such as permafrost thawing or hydrate dissociation-induced landslides, are frequently triggered by changes in thermal or hydraulic conditions [5–9]. Underpinned to these diversified processes and applications is the

* Corresponding author.
*E-mail address:* jzhao@ust.hk (J. Zhao).

https://doi.org/10.1016/j.cma.2023.116462
Received 28 May 2023; Received in revised form 10 September 2023; Accepted 16 September 2023

coupled thermo–hydro–mechanical behavior of liquid-infiltrated porous media, which is infamously challenging to model and understand either experimentally or analytically. Over the past decades, continuous efforts have been devoted to the development of advanced numerical approaches to gain a better understanding of the THM responses of saturated granular media. More recent focus has been placed on understanding large deformation and post-failure behaviors of saturated porous media subjected to multifield external loads.

Among the existing numerical methods, mesh-based methods, such as the finite element method (FEM) and the finite volume method (FVM), have been widely used for tackling multiphysics coupling problems. The Eulerian-based FVM is known to be not particularly suitable for modeling time-dependent behaviors of granular materials. FEM formulates the material motions with a Lagrangian description and has been extensively applied for the THM coupling analysis of porous media [10–18]. However, FEM is susceptible to mesh distortion in large strain regimes on a fixed mesh topology. Another alternative mesh-based method is the particle finite element method (PFEM), which employs a set of particles as nodes to discretize the continuum domain and construct a new mesh based on Delaunay triangulation [19]. The application of adaptive meshing or remeshing techniques may serve as a remedy to the mesh distortion issue but inevitably incur increased computational costs.

The past three decades also witnessed the emergence and development of various meshless or mesh-free methods that are popularly used for tackling large deformation problems. Among many, the material point method (MPM) is distinguished by its ability to leverage both the merits of mesh-based and meshless approaches, through a hybrid utilization of Lagrangian particles and Eulerian background mesh. Since proposed by Sulsky et al. [20,21], it has been effectively employed in diverse engineering and industrial scenarios that involve large deformations ranging from landslide dynamics to snow simulations [22–24]. In recent years, MPM has also been successfully extended to hydro-mechanical coupling [25–38], thermo-mechanical coupling [39–41], and more recent attempts for THM modeling [8,42]. In particular, Pinyol et al. [8] employed an explicit coupled THM MPM to investigate the dilation caused by frictional heat generation in the fast motion of landslides. Lei et al. [42] further developed an explicit generalized interpolation material point (GIMP) method to simulate the climate-driven slope failure process involving both temperature variation and rainfall infiltration. These studies help to showcase the capability of MPM in modeling the coupled response of porous media. Great varieties and diversities are also observed in these approaches, from formulations to time integration, spatial discretization, and stabilization algorithms. It remains highly desirable and practically necessary to develop a stabilized and efficient MPM featured by rigorous THM coupling to treat thermal-related large deformation engineering problems.

Two formulations are commonly followed to treat THM coupling for saturated porous media, namely, the $\boldsymbol{u}$-$p$-$T$ formulation [8] and the $\boldsymbol{u}$-$\boldsymbol{v}$-$p$-$T$ formulation [42], where $\boldsymbol{u}$, $\boldsymbol{v}$, $p$, and $T$ stand for the solid displacement, the liquid velocity, the pore pressure, and the temperature, respectively. Though widely adopted in FEM due to simplicity, the $\boldsymbol{u}$-$p$-$T$ formulation neglects the relative motions of liquid and solid phases and is hence unsuitable for fast loading and rapid motions [43]. In contrast, the $\boldsymbol{u}$-$\boldsymbol{v}$-$p$-$T$ formulation retains all features of the liquid phase and is preferable for modeling large strain and dynamic problems with high-frequency solid–liquid interactions [33,44]. Two strategies are available to solve the governing PDEs of the system: (a) monolithic scheme and (b) staggered scheme, also known as the sequential or partitioned scheme [15,18,45]. The monolithic strategy solves the system of PDEs simultaneously, whereas the staggered strategy partitions the system into several subproblems and solves each subproblem sequentially. The staggered solution schemes have been found to provide optimal rates of convergence with respect to mesh and time step refinement compared to monolithic solution schemes [46]. The applicability of different solution schemes is dependent on the degree of coupling between the thermal field and other fields [18].

MPM can be viewed as a variation of FEM in conjunction with a static finite-element mesh. Thus it suffers the same numerical problem of pathological volumetric locking and checker-boarding pressure oscillation when using low-order elements in the limit of undrained deformation or incompressible flow [13,26,47–49]. It is commonly handled by interpolating the pressure with one order lower than that of the velocity for consistency. To relax the interpolation restrictions, various stabilization schemes have been proposed, such as the reduced integration method [27,28,35], the polynomial pressure projection method [31,50,51], and the fractional step method [33,52], and among others. The fractional step method, also known as operator splitting or projection method, can fundamentally address the issue in dynamic problems with incompressible fluid limits. It decouples the unfavorable volume balance from the momentum equations by advancing each time step via intermediate steps. This allows the separation of the pore-pressure solution from the kinematical unknowns, thereby avoiding unphysical pressure oscillations [53–58].

In this study, we aim to develop stabilized MPM with an efficient staggered solution scheme for THM coupling analysis of saturated porous media. To better capture the large deformation behavior, we formulate a four-variable $\boldsymbol{u}$-$\boldsymbol{v}$-$p$-$T$ formulation in the framework of single-point two-phase MPM. To avoid using mixed-order interpolations for pressure and displacement, which is a crucial requirement in the monolithic solution scheme, we develop a staggered solution procedure where the energy equation and the hydromechanical equations are solved sequentially. To further proceed with equal order interpolations, we solve the hydromechanical part with a semi-implicit fractional step method in which some of the advantages of the pure explicit and pure implicit schemes are realized while the drawbacks are reduced. In the proposed fractional step method, we consider both the incompressible flow and the weakly compressible flow which is seldom treated in previous work. The partitioned governing equations after operator-splitting are spatially discretized following standard GIMP procedure. Axisymmetric forms of the THM-coupled MPM are also derived to facilitate efficiently solving such axisymmetric problems that are common in thermal-related engineering settings [59–61]. Solution procedures for the fully explicit method are also presented as complementation of its semi-implicit counterpart. To the best of our knowledge, this is the first attempt at developing an oscillation-free and relatively computational-efficient THM-coupled GIMP method for solving a wide range of problems, from multidimensional to axisymmetric problems, from weakly compressible flow to incompressible flow, and most importantly, from small deformations to large deformations.

The manuscript is structured as follows. Section 2 presents the governing equations for THM-coupled problems in saturated porous

media. Section 3 presents the numerical schemes, including the temporal integration scheme, spatial discretization, and the completed solution procedures. In Section 4, we validate the proposed formulations by conducting three benchmark examples. In Section 5, we further conduct an engineering application problem involving large deformation, focusing on the failure of a slope caused by temperature changes. Section 6 gives some concluding summaries.

## 2. Governing equations

The governing equations for a fully coupled THM system of saturated porous media are derived in the framework of single-point two-phase MPM based on ***u-v-p-T*** formulation as outlined in the following.

### 2.1. Volume fractions, partial stresses, and strains

According to the theory of mixture [62,63], each phase $\alpha \in \{s, l\}$ (solid, liquid) in a representative volume element (RVE) of a saturated porous medium is characterized by its volume fraction $n_\alpha$, and the partial density $\overline{\rho}_\alpha$ of each phase is characterized by the average density with the volume fraction, which read,

$$n_\alpha = \frac{\mathrm{d}V_\alpha}{\mathrm{d}V}, \qquad \overline{\rho}_\alpha = n_\alpha \rho_\alpha, \qquad \rho_m = n_s\rho_s + n_l\rho_l = (1-n)\rho_s + n\rho_l \tag{1}$$

where $\mathrm{d}V$ is the volume of the RVE, $\mathrm{d}V_\alpha$ is the volume of $\alpha$ phase, $\rho_\alpha$ is the intrinsic density of $\alpha$ phase, $\rho_m$ is the average density of the mixture, and $n$ is the porosity, interchangeable with the liquid volume fraction $n_l$.

In mixture theory, the partial stress $\boldsymbol{\sigma}_s$ and $\boldsymbol{\sigma}_l$ on solids and liquids are defined as follows [64,65],

$$\boldsymbol{\sigma}_s = \boldsymbol{\sigma}^{'} - n_s p\boldsymbol{I}, \qquad \boldsymbol{\sigma}_l = -n_l p\boldsymbol{I} \tag{2}$$

where $p$ is the pore liquid pressure (assumed to be positive in compression), $\boldsymbol{\sigma}^{'}$ is the effective stress (positive in tension), and $\boldsymbol{I}$ is the identity tensor. The effective stress theory is utilized to characterize the coupled mechanics of the solid skeleton and the liquid, in which the total stress tensor $\boldsymbol{\sigma}$ is expressed as the sum of the stress of each phase,

$$\boldsymbol{\sigma} = \boldsymbol{\sigma}^{'} - p\boldsymbol{I} \tag{3}$$

The effective stress of the solid is then linked with its strain by a constitutive law. For non-isothermal conditions, the constitutive relation considering the thermal effect is expressed as,

$$\dot{\boldsymbol{\sigma}}^{'} = \boldsymbol{D} : \dot{\boldsymbol{\varepsilon}}, \qquad \text{with } \dot{\boldsymbol{\varepsilon}} = \dot{\boldsymbol{\varepsilon}}_s + \dot{\boldsymbol{\varepsilon}}_T \tag{4}$$

where $\dot{\boldsymbol{\sigma}}^{'}$ is the rate of effective stress, $\dot{\boldsymbol{\varepsilon}}$ is the rate of total strain, $\boldsymbol{D}$ is the tangent matrix that defines the relationship between the effective stress and the strain, and $\dot{\boldsymbol{\varepsilon}}_s$ and $\dot{\boldsymbol{\varepsilon}}_T$ are the rate of mechanical strain and thermal strain, respectively, calculated by,

$$\dot{\boldsymbol{\varepsilon}}_s = \left(\boldsymbol{L}_s + \boldsymbol{L}_s^T\right)/2 \tag{5a}$$

$$\dot{\boldsymbol{\varepsilon}}_T = -\beta_s \dot{T}\boldsymbol{I} \tag{5b}$$

where $\boldsymbol{L}_s = \nabla \boldsymbol{v}_s$ is the velocity gradient, $\boldsymbol{v}_s$ is the solid velocity, $\dot{T}$ is the time derivative of temperature, and $\beta_s$ is the volumetric thermal expansivity of solids.

### 2.2. Conservation of mass

In single-point multi-phase MPM, all constituents are represented by the same Lagrangian material point in the current configuration. By considering an Eulerian description for the liquid with the solid being a reference, the material time derivative of the liquid phase is described with respect to the motion of the solid phase as follows,

$$\frac{\mathrm{D}_l(*)}{\mathrm{D}t} = \frac{\mathrm{D}_s(*)}{\mathrm{D}t} + (\boldsymbol{v}_l - \boldsymbol{v}_s)\cdot\nabla(*) \tag{6}$$

where $\boldsymbol{v}_\alpha$ is the velocity and $\frac{\mathrm{D}_\alpha(*)}{\mathrm{D}t} = \frac{\partial(*)}{\partial t} + \boldsymbol{v}_\alpha\nabla(*)$ is the material time derivative of $(*)$ regarding $\alpha$ phase.

By assuming there is no phase transition between constituents, the mass balance equations for solid and liquid phases are written as,

$$\frac{\mathrm{D}_s\overline{\rho}_s}{\mathrm{D}t} + \overline{\rho}_s\nabla\cdot\boldsymbol{v}_s = 0 \tag{7a}$$

$$\frac{\mathrm{D}_s\overline{\rho}_l}{\mathrm{D}t}+(\boldsymbol{v}_l-\boldsymbol{v}_s)\cdot\nabla\overline{\rho}_l+\overline{\rho}_l\nabla\cdot\boldsymbol{v}_l=0 \tag{7b}$$

In view of $n_s+n_l=1$, the mass balance equation of the solid–liquid mixture can be formulated as,

$$\frac{n_s}{\rho_s}\frac{\mathrm{D}_s\rho_s}{\mathrm{D}t}+\frac{n_l}{\rho_l}\frac{\mathrm{D}_s\rho_l}{\mathrm{D}t}+\frac{1}{\rho_l}(\boldsymbol{v}_l-\boldsymbol{v}_s)\cdot\nabla\overline{\rho}_l+n_s\nabla\cdot\boldsymbol{v}_s+n_l\nabla\cdot\boldsymbol{v}_l=0 \tag{8}$$

Further development of Eq. (8) requires state equations that relate the intrinsic density to pressure and temperature [11]. The required relationship is derived based on the truncated Taylor series expansion, expressed as follows,

$$\frac{1}{\rho_\alpha}\frac{\mathrm{D}_s\rho_\alpha}{\mathrm{D}t}=-\beta_\alpha\frac{\mathrm{D}_sT}{\mathrm{D}t}+\gamma_\alpha\frac{\mathrm{D}_sp_\alpha}{\mathrm{D}t} \tag{9}$$

where $\beta_\alpha=-\frac{1}{\rho_\alpha}\frac{\partial\rho_\alpha}{\partial T}$ and $\gamma_\alpha=\frac{1}{\rho_\alpha}\frac{\partial\rho_\alpha}{\partial p_\alpha}$, defined as the coefficients of thermal expansion and compressibility, respectively, $T$ is the temperature of the mixture, and $p_\alpha$ is the pressure on $\alpha$ phase. In the balance of mass, the influence of solid compressibility is not considered (i.e., $\gamma_s=0$). Substituting the state equation of each phase into Eq. (8) and neglecting the spatial difference of liquid density (i.e., $\nabla\rho_l=0$) yield the following balance equation of mass of mixture,

$$-\beta_m\frac{\mathrm{D}_sT}{\mathrm{D}t}+n_l\gamma_l\frac{\mathrm{D}_sp}{\mathrm{D}t}+n_l\nabla\cdot\boldsymbol{v}_l+n_s\nabla\cdot\boldsymbol{v}_s=0 \tag{10}$$

where $\beta_m=n_s\beta_s+n_l\beta_l$.

### 2.3. Conservation of momentum

The motion of the liquid-saturated porous media is controlled by the momentum balance equations for the solid phase and the liquid phase, respectively,

$$\overline{\rho}_s\frac{\mathrm{D}_s\boldsymbol{v}_s}{\mathrm{D}t}=\nabla\cdot\boldsymbol{\sigma}_s+\overline{\rho}_s\boldsymbol{b}+\boldsymbol{f}_s \tag{11a}$$

$$\overline{\rho}_l\frac{\mathrm{D}_s\boldsymbol{v}_l}{\mathrm{D}t}+\overline{\rho}_l(\boldsymbol{v}_l-\boldsymbol{v}_s)\nabla\cdot\boldsymbol{v}_l=\nabla\cdot\boldsymbol{\sigma}_l+\overline{\rho}_s\boldsymbol{b}+\boldsymbol{f}_l \tag{11b}$$

where $\boldsymbol{\sigma}_\alpha$ is the Cauchy stress tensor of $\alpha$ phase, defined in Eq. (2), $\boldsymbol{b}$ is the body force vector, and $\boldsymbol{f}_\alpha$ is the interaction force vector between phase $\alpha$ and other phases. The exchange of momenta between solid and liquid constituents is an internal behavior. Thus, the sum of the interaction forces of all phases is zero, i.e., $\sum_\alpha\boldsymbol{f}_\alpha=0$. The convective term $\overline{\rho}_l(\boldsymbol{v}_l-\boldsymbol{v}_s)\nabla\cdot\boldsymbol{v}_l$ in Eq. (11b) is small compared to the interaction force, thereby being neglected [52,65]. The momentum balance equation for the mixture can be obtained by summing the equation of each constituent as follows,

$$\overline{\rho}_s\frac{\mathrm{D}_s\boldsymbol{v}_s}{\mathrm{D}t}+\overline{\rho}_l\frac{\mathrm{D}_s\boldsymbol{v}_l}{\mathrm{D}t}=\nabla\cdot(\boldsymbol{\sigma}'-p\boldsymbol{I})+\rho_m\boldsymbol{b} \tag{12}$$

Assuming that the pore fluid is laminar and fulfills Darcy's law for either small or large deformation conditions [8,42], the interaction force vectors are calculated by,

$$\boldsymbol{f}_s=-\boldsymbol{f}_l=-p\nabla n_l+n_l^2\frac{\rho_l g}{k}(\boldsymbol{v}_l-\boldsymbol{v}_s) \tag{13}$$

where $g$ is the gravitational acceleration, and $k$ is the hydraulic conductivity. $p\nabla n_l$ is the so-called buoyance force, and $n_l^2\frac{\rho_l g}{k}(\boldsymbol{v}_l-\boldsymbol{v}_s)$ is the drag force. Note that the assumption of laminar flow is valid on the concept of average, implying that the pore fluid may be in a turbulent state somewhere but overall displays a laminar flow in an RVE.

By substituting Eq. (13) into Eq. (11a), the final expression of the momentum balance equation for each phase can be formulated as,

$$\overline{\rho}_s\frac{\mathrm{D}_s\boldsymbol{v}_s}{\mathrm{D}t}=\nabla\cdot\boldsymbol{\sigma}'-n_s\nabla p+\overline{\rho}_s\boldsymbol{b}+n_l^2\frac{\rho_l g}{k}(\boldsymbol{v}_l-\boldsymbol{v}_s) \tag{14a}$$

$$\overline{\rho}_l\frac{\mathrm{D}_s\boldsymbol{v}_l}{\mathrm{D}t}=-n_l\nabla p+\overline{\rho}_l\boldsymbol{b}-n_l^2\frac{\rho_l g}{k}(\boldsymbol{v}_l-\boldsymbol{v}_s) \tag{14b}$$

### 2.4. Conservation of energy

Assuming the temperature in an RVE is uniform for both the liquid and the solid and there is no phase transition between components, the energy balance equation for each phase can be formulated as,

$$\overline{\rho}_s c_s \frac{\mathrm{D}_s T}{\mathrm{D}t} + \nabla \cdot \boldsymbol{\phi}_s = Q_s \tag{15a}$$

$$\overline{\rho}_l c_l \frac{\mathrm{D}_s T}{\mathrm{D}t} + \overline{\rho}_l c_l (\boldsymbol{v}_l - \boldsymbol{v}_s) \cdot \nabla T + \nabla \cdot \boldsymbol{\phi}_l = Q_l \tag{15b}$$

where $c_\alpha$ is the specific heat capacity, $\boldsymbol{\phi}_\alpha$ is the conductive heat flux, and $Q_\alpha$ is the heat source. $\boldsymbol{\phi}_\alpha$ is computed based on Fourier's law,

$$\boldsymbol{\phi}_\alpha = -n_\alpha \boldsymbol{\kappa}_\alpha \nabla T \tag{16}$$

where $\boldsymbol{\kappa}_\alpha$ is the coefficient tensor of thermal conductivity. For simplification, the thermal conductivity is assumed to be isotropic. Eqs. (15a) and (15b) are finally combined into one single equation for the porous medium as a whole,

$$C_m \frac{\mathrm{D}_s T}{\mathrm{D}t} + \overline{\rho}_l c_l (\boldsymbol{v}_l - \boldsymbol{v}_s) \cdot \nabla T + \nabla \cdot (-\kappa_m \nabla T) = Q \tag{17}$$

where $C_m = n_l \rho_l c_l + n_s \rho_s c_s$, $\kappa_m = n_l \kappa_l + n_s \kappa_s$, and $Q$ is the heat source of the system. The heat source $Q$ is present in diverse circumstances such as plastic dissipation ($= \theta \boldsymbol{\sigma}' : \dot{\boldsymbol{\epsilon}}^p$, where $\dot{\boldsymbol{\epsilon}}^p$ is the plastic strain rate, and $\theta$ is the coefficient of plastic work transferring into heat dissipation), and the convective or radiative heat from external sources. It should be noted that although plastic dissipation is not a focus of current work, the treatment of this coupling term as a source term is nontrivial since it may destabilize the heat equation numerically [66,67]. Readers may refer to the relative works on how to treat the plasticity term in loose or tight coupling conditions [8,40,42,68,69].

### 2.5. Boundary conditions

The $n$-dimensional domain in the current configuration is denoted by $\Omega \in \mathbb{R}^n$, and the boundary of the domain is denoted by $\partial\Omega$. The boundary is decomposed into the velocity boundary $\partial_v\Omega$, the pore pressure boundary $\partial_p\Omega$, the temperature boundary $\partial_T\Omega$, the traction boundary $\partial_t\Omega$, the Darcy flux boundary $\partial_q\Omega$, and the heat flux boundary $\partial_\phi\Omega$. The time dimension of the problem is denoted by $\mathscr{T} = (0, T]$ with $T > 0$. Together with the above governing equations, a general problem is collectively subjected to the following boundary conditions,

$$\boldsymbol{v}_\alpha = \widehat{\boldsymbol{v}}_\alpha \text{ on } \partial_v\Omega \times \mathscr{T} \tag{18a}$$

$$p = \widehat{p} \text{ on } \partial_p\Omega \times \mathscr{T} \tag{18b}$$

$$T = \widehat{T} \text{ on } \partial_T\Omega \times \mathscr{T} \tag{18c}$$

$$\boldsymbol{\sigma} \cdot \boldsymbol{n} = \widehat{\boldsymbol{t}} \text{ on } \partial_t\Omega \times \mathscr{T} \tag{18d}$$

$$-\boldsymbol{q} \cdot \boldsymbol{n} = \widehat{q} \text{ on } \partial_q\Omega \times \mathscr{T} \tag{18e}$$

$$-\boldsymbol{\phi} \cdot \boldsymbol{n} = \widehat{\phi} \text{ on } \partial_h\Omega \times \mathscr{T} \tag{18f}$$

where $\widehat{\boldsymbol{v}}_\alpha$, $\widehat{p}$, and $\widehat{T}$ are the prescribed boundary velocity, pore pressure, and temperature on $\partial_v\Omega$, $\partial_p\Omega$, and $\partial_T\Omega$, respectively, and $\widehat{\boldsymbol{t}}$, $\widehat{q}$, and $\widehat{\phi}$ are the prescribed traction vector, Darcy flux, and heat flux on $\partial_t\Omega$, $\partial_q\Omega$, and $\partial_\phi\Omega$, respectively. Eqs. (18a), (18b), and (18c) are the Dirichlet boundary conditions, and Eqs. (18d), (18e), and (18f) are the Neumann boundary conditions.

## 3. Numerical schemes for THM-coupled MPM

To balance the numerical stability and the computational efficiency, a staggered solution scheme is adopted to solve the coupled equations. The temperature is first solved with explicit time integration while other variables remain constant, and the remaining kinematical unknowns are advanced with the updated temperature using a semi-implicit fractional step method. The spatial discretization of the partitioned governing equations follows the standard GIMP method.

### 3.1. Temporal discretization

The choice of a staggered solution scheme is motivated by the following considerations. The implicit monolithic solution scheme requires the use of mixed-order finite elements to avoid the volumetric locking and the spurious pressure field. This is not preferable for MPM as all the standard MPM formulations are low order. Besides, the rate of convergence for the monolithic solution scheme is also a problem in MPM simulation where the large deformation dominates. In geotechnical engineering, the temperature usually changes at a low rate, which makes it a weak coupling with the kinematical variables. Thus, it is accessible to partition the fully coupled equations into two subsets to promote a weak coupling between thermal fields and hydro-mechanical fields. Finally, the utilization of the operator-splitting technique further decouples the pore pressure and kinematical variables in the momentum equations to facilitate the equal-order interpolation of pressure and displacement fields in MPM. Previous practices in FEMs indicate that the strategy offers a satisfactory convergence rate and accuracy [18,46].

The energy balance equation is solved by the explicit forward Euler scheme,

$$C_m\frac{T^{k+1}-T^k}{\Delta t}=-\overline{\rho}_l c_l\left(\boldsymbol{v}_l^k-\boldsymbol{v}_s^k\right)\cdot\nabla T^k-\nabla\cdot\left(-\kappa_m\nabla T^k\right)+Q \tag{19}$$

where the superscript $k$ and $k+1$ represent the current time step and next time step, and $\Delta t$ is the time step size. The explicit scheme is cost-efficient, and the solution is adequately accurate for simulating the heat transfer in porous media in engineering problems.

The fractional step scheme is implemented by splitting the momentum equation into a predicting step and a correcting step with the predicted velocity $\boldsymbol{v}_\alpha^*$ as an intermediate variable. The split momentum equations for velocity predicting are obtained as,

$$\overline{\rho}_s\frac{\boldsymbol{v}_s^*-\boldsymbol{v}_s^k}{\Delta t}+\overline{\rho}_l\frac{\boldsymbol{v}_l^*-\boldsymbol{v}_l^k}{\Delta t}=\nabla\cdot\left(\boldsymbol{\sigma}'^k-p^k\boldsymbol{I}\right)+\rho_m\boldsymbol{b} \tag{20a}$$

$$\overline{\rho}_l\frac{\boldsymbol{v}_l^*-\boldsymbol{v}_l^k}{\Delta t}=-n_l\nabla p^k+\overline{\rho}_l\boldsymbol{b}-n_l^2\frac{\rho_l g}{k}\left(\boldsymbol{v}_l^*-\boldsymbol{v}_s^*\right) \tag{20b}$$

and the correcting step for each phase is obtained as,

$$\overline{\rho}_\alpha\frac{\boldsymbol{v}_\alpha^{k+1}-\boldsymbol{v}_\alpha^*}{\Delta t}=-n_\alpha\nabla\left(p^{k+1}-p^k\right) \tag{21}$$

Substituting Eq. (21) into the mass balance equation yields the pressure Poisson equation,

$$\Delta t\xi\nabla^2\left(p^{k+1}-p^k\right)-n_l\gamma_l\frac{p^{k+1}-p^k}{\Delta t}=n_l\nabla\cdot\boldsymbol{v}_l^*+n_s\nabla\cdot\boldsymbol{v}_s^*-\beta_m\frac{T^{k+1}-T^k}{\Delta t} \tag{22}$$

where $\xi=n_s/\rho_s+n_l/\rho_l$. Note that the pore pressure is implicitly evaluated by solving the pressure Poisson equation, while the stress is still evaluated explicitly to avoid iteration associated with the elastoplastic stiffness matrix. It is also worth noting that in the previous fractional step scheme, the liquid phase in porous media is usually assumed to be incompressible (i.e., $\gamma_l=0$), whereas in the presented formulation, the liquid can be weakly compressible (i.e., $\gamma_l\neq 0$). The numerical results for incompressible and weakly compressible fractional step methods are compared in the numerical cases.

Since the temperature equation is solved with explicit time stepping, the time interval should fulfill the Courant–Friedrichs–Levy (CFL) condition. The CFL condition for the energy equation is controlled by the thermal diffusivity of the porous media as follows,

$$\Delta t_{crit,T}<l_{min}^2/c_T \tag{23}$$

where $l_{min}$ is the minimum element size, and $c_T=\kappa_m/C_m$ is the thermal diffusivity. Also, due to the explicit treatment for effective stress in Eq. (20a), the time step size for saturated elastic media in undrained conditions is constrained by the elastic wave propagation speed, given by,

$$\Delta t_{crit,u}<l_{min}/c_u \tag{24}$$

where $c_u=\sqrt{E(1-\nu)/[\rho_m(1+\nu)(1-2\nu)]}$ is the elastic compressional wave speed in the porous medium, and $E$ and $\nu$ are the elastic modulus and the Poisson's ratio, respectively. Since the drag force is evaluated implicitly, the critical time step size is not limited by the permeability [70].

### 3.2. Weak form

To apply MPM discretization, the semi-discrete equations are transformed into weak form based on the standard Galerkin procedure. Considering the boundary conditions in Eq. (18), the virtual work equations can be obtained by multiplying corresponding equations with test functions $\delta T$ (with zeros on $\partial_T\Omega$), $\delta \boldsymbol{v}$ (with zeros on $\partial_v\Omega$), and $\delta p$ (with zeros on $\partial_p\Omega$), respectively, and integrating over the whole domain $\Omega$.

After applying the integral by part and the divergence theorem, the weak form of the energy balance equation is obtained as,

$$\int_\Omega \delta T \cdot C_m \dot{T}^{k+1} \mathrm{d}V = -\int_\Omega \delta T \cdot \overline{\rho}_l c_l \left(\boldsymbol{v}_l^k - \boldsymbol{v}_s^k\right) \nabla T \mathrm{d}V + \int_\Omega \nabla \delta T \cdot (-\kappa_m \nabla T) \mathrm{d}V - \int_{\partial\Omega_h} \delta T \cdot \widehat{\phi} \mathrm{d}S + \int_\Omega \delta T \cdot Q \mathrm{d}V \tag{25}$$

where $\widehat{\phi}$ is the prescribed boundary heat flux defined in Eq. (18f).

By the same procedure, the weak form of the predicting step of momentum equations can be written as,

$$\int_\Omega \delta \boldsymbol{v} \cdot \frac{\overline{\rho}_s}{\Delta t}\left(\boldsymbol{v}_s^* - \boldsymbol{v}_s^k\right) \mathrm{d}V + \int_\Omega \delta \boldsymbol{v} \cdot \frac{\overline{\rho}_l}{\Delta t}\left(\boldsymbol{v}_l^* - \boldsymbol{v}_l^k\right) \mathrm{d}V = \int_{\partial\Omega} \delta \boldsymbol{v} \cdot \widehat{\boldsymbol{t}} \mathrm{d}S - \int_\Omega \nabla \delta \boldsymbol{v} : \left(\boldsymbol{\sigma}'^k - p^k \boldsymbol{I}\right) \mathrm{d}V + \int_\Omega \delta \boldsymbol{v} \cdot \rho_m \boldsymbol{b} \mathrm{d}V \tag{26a}$$

$$\int_\Omega \delta \boldsymbol{v} \cdot \frac{\overline{\rho}_l}{\Delta t}\left(\boldsymbol{v}_l^* - \boldsymbol{v}_l^k\right) \mathrm{d}V + \int_\Omega \delta \boldsymbol{v} \cdot n_l^2 \frac{\rho_l g}{k}\left(\boldsymbol{v}_l^* - \boldsymbol{v}_s^*\right) \mathrm{d}V = \int_{\partial\Omega} \delta \boldsymbol{v} \cdot (-n_l \widehat{p} \boldsymbol{I}) \cdot \boldsymbol{n} \mathrm{d}S - \int_\Omega \nabla \delta \boldsymbol{v} : \left(-n_l p^k \boldsymbol{I}\right) \mathrm{d}V + \int_\Omega \delta \boldsymbol{v} \cdot \overline{\rho}_l \boldsymbol{b} \mathrm{d}V \tag{26b}$$

where $\widehat{\boldsymbol{t}}$ and $\widehat{p}$ are boundary traction force and boundary pore pressure defined in Eq. (18).

Similarly, the weak form of the correcting step of momentum equations can be written as,

$$\int_\Omega \delta \boldsymbol{v} \cdot \frac{\overline{\rho}_\alpha}{\Delta t}\left(\boldsymbol{v}_\alpha^{k+1} - \boldsymbol{v}_\alpha^*\right) \mathrm{d}V = -\int_\Omega \delta \boldsymbol{v} \cdot n_\alpha \nabla\left(p^{k+1} - p^k\right) \mathrm{d}V \tag{27}$$

The final one is the weak form of the pressure Poisson equation, which can be written as,

$$\begin{aligned} &\int_\Omega \nabla \delta p \cdot \Delta t \xi \nabla\left(p^{k+1} - p^k\right) \mathrm{d}V + \int_\Omega \delta p \cdot n_l \gamma_l \Delta t^{-1}\left(p^{k+1} - p^k\right) \mathrm{d}V \\ &= \int_\Omega \delta p \cdot \beta_m \dot{T}^{k+1} \mathrm{d}V + \int_\Omega \nabla \delta p \cdot n_s \boldsymbol{v}_s^* \mathrm{d}V - \int_{\partial\Omega} \delta p \cdot n_s \boldsymbol{v}_s^* \cdot \boldsymbol{n} \mathrm{d}S \\ &+ \int_\Omega \nabla \delta p \cdot n_l \boldsymbol{v}_l^* \mathrm{d}V - \int_{\partial\Omega} \delta p \cdot n_l \boldsymbol{v}_l^* \cdot \boldsymbol{n} \mathrm{d}S + \int_{\partial\Omega} \delta p \cdot \xi \Delta t \nabla\left(p^{k+1} - p^k\right) \cdot \boldsymbol{n} \mathrm{d}S \end{aligned} \tag{28}$$

Here, the variational form of the pressure Poisson equation is obtained with an artificial Neumann boundary condition $\nabla\left(p^{k+1} - p^k\right) \cdot \boldsymbol{n}$, which is not required in the original balance equations. For drained and undrained conditions, this artificial incremental pressure gradient boundary can be simplified as $\nabla\left(p^{k+1} - p^k\right) \cdot \boldsymbol{n} = 0$, which is found to be automatically enforced by setting $\boldsymbol{v}_l^* \cdot \boldsymbol{n} = 0$ [33]. More numerical issues related to the implementation of artificial pressure gradient boundary in the projection method can be found in previous work on the Navior-stokes equation [71,72].

### 3.3. Spatial discretization

The semi-discrete weak formulations are then discretized in space based on MPM. Compared to FEM, the main difference is that the numerical integrations in the MPM are performed at the moving material points instead of fixed quadratures. In the original MPM, the spatial interpolation functions are identical to standard FE shape functions. To reduce the numerical noise when material points cross the cell boundary in the original MPM, the generalized interpolation material point (GIMP) method was developed by Bardenhagen and Kober [73] and adopted in this study in case of large deformation problems. In the GIMP method, the grid shape function $N_i(\boldsymbol{x})$ is smoothed via the particle characteristic function $\chi_p(\boldsymbol{x})$ as follows,

$$S_{ip} = \frac{1}{V_p}\int_{\Omega_p \cap \Omega} \chi_p(\boldsymbol{x}) N_i(\boldsymbol{x}) \mathrm{d}V, \qquad \nabla S_{ip} = \frac{1}{V_p}\int_{\Omega_p \cap \Omega} \chi_p(\boldsymbol{x}) \nabla N_i(\boldsymbol{x}) \mathrm{d}V \tag{29}$$

where $S_{ip}$ is the smoothed shape function, or called the weighing function, $\nabla S_{ip}$ is its spatial gradient, $i$ and $p$ denote 'node' and 'material point (particle)', respectively, $\Omega$ and $\Omega_p$ are the material domain and the influence domain of material point $p$, and $V_p = \int_{\Omega_p} \chi_p(\boldsymbol{x}) \mathrm{d}V$ is the material point volume. In this study, the linear shape functions are used for both pressure and displacement interpolations.

With the weighing functions, the integral equations can be further discretized into summation forms. For the energy balance equation, the discretized equation can be written in the following compact form,

$$\mathscr{C}\dot{\mathscr{T}}^{k+1} = \mathscr{E}^{int} + \mathscr{E}^{ext} \tag{30}$$

with

$$\mathscr{C} = \sum_p \boldsymbol{S}_p^T C_{mp} \boldsymbol{S}_p \tag{31a}$$

$$\mathscr{E}^{int} = -\sum_p \boldsymbol{S}_p^T V_p \overline{\rho}_l c_l \left( \boldsymbol{v}_{lp}^k - \boldsymbol{v}_{sp}^k \right) \nabla T_p^k - \sum_p \nabla \boldsymbol{S}_p^T V_p \kappa_m \nabla T_p^k \tag{31b}$$

$$\mathscr{E}^{ext} = \sum_p \boldsymbol{S}_p^T V_p Q + \sum_p \boldsymbol{S}_p^T V_p h^{-1} \overline{\boldsymbol{\phi}} \tag{31c}$$

where $\dot{\mathscr{T}}^{k+1}$ is the array of nodal temperature rate $\dot{T}_i^{k+1}$, $\mathscr{C}$ is the matrix of nodal heat capacity, $\mathscr{E}^{int}$ and $\mathscr{E}^{ext}$ are the arrays of nodal internal and external heats, respectively, $h$ is the fictitious boundary thickness, $\boldsymbol{S}_p$ is the array of above-defined interpolation functions with regard to material point $p$, and $\boldsymbol{S}_p^T$ is the transpose of $\boldsymbol{S}_p$. To facilitate explicit integration, the lumped matrix is used for $\mathscr{C}$.

Similarly, the momentum balance equations can be discretized as,

$$\begin{cases} \mathscr{M}_s \left( \boldsymbol{\nu}_s^* - \boldsymbol{\nu}_s^k \right) + \mathscr{M}_l \left( \boldsymbol{\nu}_l^* - \boldsymbol{\nu}_l^k \right) = \mathscr{F}_m^{int} + \mathscr{F}_m^{ext} \\ \mathscr{M}_l \left( \boldsymbol{\nu}_l^* - \boldsymbol{\nu}_l^k \right) + \mathscr{F}^d \left( \boldsymbol{\nu}_l^* - \boldsymbol{\nu}_s^* \right) = \mathscr{F}_l^{int} + \mathscr{F}_l^{ext} \end{cases} \tag{32}$$

and

$$\begin{cases} \mathscr{M}_s \left( \boldsymbol{\nu}_s^{k+1} - \boldsymbol{\nu}_s^* \right) = -\mathscr{F}_s^{cor} \Delta \boldsymbol{\nu}^{k+1} \\ \mathscr{M}_l \left( \boldsymbol{\nu}_l^{k+1} - \boldsymbol{\nu}_l^* \right) = -\mathscr{F}_l^{cor} \Delta \boldsymbol{\nu}^{k+1} \end{cases} \tag{33}$$

with

$$\mathscr{M}_\alpha = \sum_p \boldsymbol{S}_p^T V_p \overline{\rho}_\alpha \Delta t^{-1} \boldsymbol{S}_p \tag{34a}$$

$$\mathscr{F}_m^{int} = -\sum_p \nabla \boldsymbol{S}_p^T : V_p \left( \boldsymbol{\sigma}_p'^k - p_p^k \boldsymbol{I} \right) \tag{34b}$$

$$\mathscr{F}_m^{ext} = \sum_p \boldsymbol{S}_p^T V_p h^{-1} \widehat{\boldsymbol{t}}_p + \sum_p \boldsymbol{S}_p^T V_p \rho_m \boldsymbol{b}_p \tag{34c}$$

$$\mathscr{F}_l^{int} = -\sum_p \nabla \boldsymbol{S}_p^T : V_p \left( -n_{lp} p_p^k \boldsymbol{I} \right) \tag{34d}$$

$$\mathscr{F}_l^{ext} = \sum_p \boldsymbol{S}_p^T V_p h^{-1} \left( -n_l \widehat{p^k} \boldsymbol{I} \right) \cdot \boldsymbol{n} + \sum_p \boldsymbol{S}_p^T V_p \overline{\rho}_l \boldsymbol{b}_p \tag{34e}$$

$$\mathscr{F}^d = \sum_p \boldsymbol{S}_p^T V_p n_{lp}^2 \frac{\rho_l g}{k} \boldsymbol{S}_p \tag{34f}$$

$$\mathscr{F}_\alpha^{cor} = \sum_p \boldsymbol{S}_p^T V_p n_{\alpha p} \nabla \boldsymbol{S}_p \tag{34g}$$

where $\boldsymbol{\nu}_\alpha^*$, $\boldsymbol{\nu}_\alpha^k$, $\boldsymbol{\nu}_\alpha^{k+1}$, and $\Delta \boldsymbol{\nu}^{k+1}$ are the nodal arrays of $\boldsymbol{v}_{\alpha j}^*$, $\boldsymbol{v}_{sj}^k$, $\boldsymbol{v}_{\alpha j}^{k+1}$, and $\Delta p_j^{k+1}$, respectively, and $\mathscr{M}_\alpha$, $\mathscr{F}^d$, $\mathscr{F}_\alpha^{int}$, $\mathscr{F}_\alpha^{ext}$, and $\mathscr{F}_\alpha^{cor}$ are the

nodal matrices associated with mass, drag force, internal force, external force, and corrected force, respectively.

Finally, the discretized pressure Poisson equation can be written as,

$$\mathscr{L}\Delta\boldsymbol{p}^{k+1} = \mathscr{B}\dot{\mathscr{T}}^{k+1} + \mathscr{N}_s\boldsymbol{e}_s^* + \mathscr{N}_l\boldsymbol{e}_l^* \tag{35}$$

with

$$\mathscr{L} = \sum_p \nabla \boldsymbol{S}_p^T V_p \Delta t \xi \nabla \boldsymbol{S}_p + \sum_p \boldsymbol{S}_p^T V_p n_{lp} \gamma_{lp} \Delta t^{-1} \boldsymbol{S}_p \tag{36a}$$

$$\mathscr{B} = \sum_p \boldsymbol{S}_p^T V_p \beta_{mp} \boldsymbol{S}_p \tag{36b}$$

$$\mathscr{N}_\alpha = \sum_p \nabla \boldsymbol{S}_p^T V_p n_{\alpha p} \boldsymbol{S}_p \tag{36c}$$

where $\mathscr{L}$, $\mathscr{A}$, $\mathscr{B}$, and $\mathscr{N}_\alpha$ are the nodal coefficient matrices of Laplacian multiplier, liquid compressibility, thermal expansion, and volume fraction.

### 3.4. Solution procedure

The typical procedure of MPM includes four main stages, as illustrated in Fig. 1. Detailed solution procedure for the semi-implicit THM-coupled MPM is presented in Section 3.4.1. For comparison, we also depict the solution procedure for explicit THM-coupled MPM and highlight the main differences between the two methods in Section 3.4.2. The proposed framework is implemented based on the open-source CB-Geo MPM code [74].

#### 3.4.1. Semi-implicit THM-coupled MPM

Fig. 2 illustrates the solution procedure of the semi-implicit THM-coupled MPM. Each sub-step is carried out as follows.

(1) Assign the initial material point properties $\rho_{\alpha p}^0$, $V_p^0$, $n_{\alpha p}^0$, $\boldsymbol{v}_{\alpha p}^0$, $T_p^0$, $\boldsymbol{\sigma}_p'^0$, and $p_p^0$.

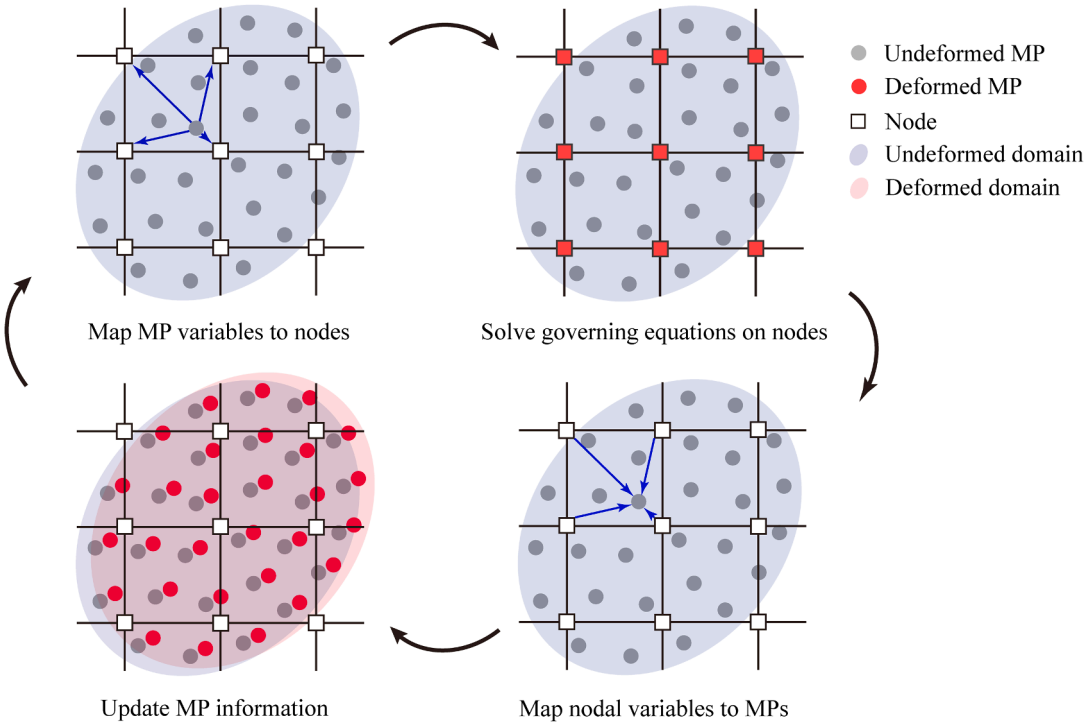


**Fig. 1.** Illustration of typical MPM procedure.

(2) Initialize MPM background mesh and compute shape functions.

(3) Map the mass, momentum, heat capacity, and heat from material points to nodes, and compute nodal velocity $\boldsymbol{v}_{\alpha i}^{k}$ and nodal temperature $T_i^k$ by,

$$\boldsymbol{v}_{\alpha i}^{k} = \sum_p m_{\alpha p}^{k} \boldsymbol{v}_{\alpha p}^{k} S_{ip} \Big/ \sum_p m_{\alpha p}^{k} S_{ip} \tag{37}$$

$$T_i^k = \sum_p V_p^k C_{mp}^k T_p^k S_{ip} \Big/ \sum_p V_p^k C_{mp}^k S_{ip} \tag{38}$$

(4) Compute the velocity gradient of material points based on the mapped nodal velocities, and then calculate particle incremental total stain $\Delta\boldsymbol{\varepsilon}_p^{k+1}$,

$$\Delta\boldsymbol{\varepsilon}_p^{k+1} = \frac{1}{2}\left[\boldsymbol{L}_{sp}^{k} + \left(\boldsymbol{L}_{sp}^{k}\right)^{T}\right] - \beta_s \Delta T_p^k \boldsymbol{I} \tag{39}$$

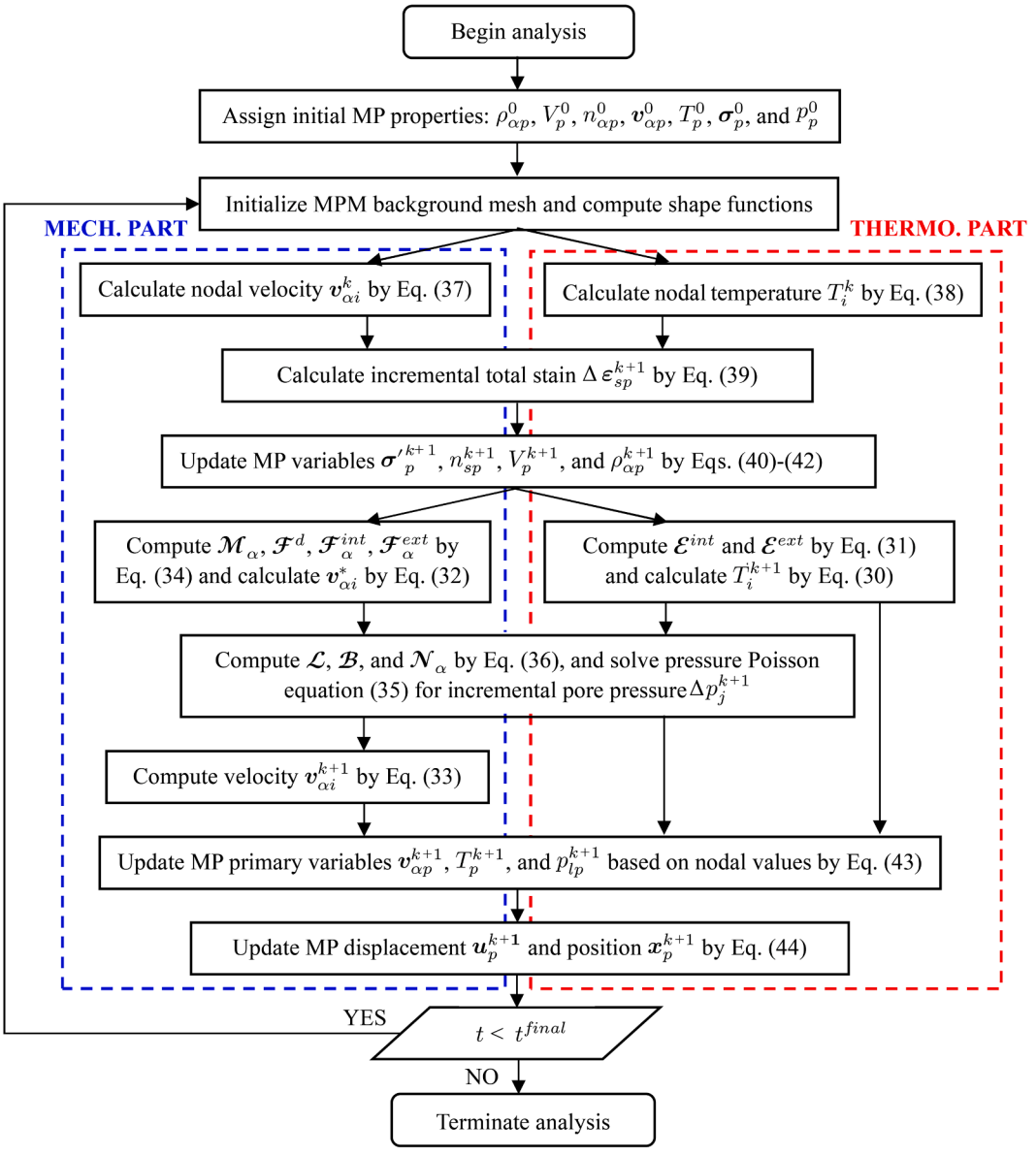


**Fig. 2.** Solution procedure of the semi-implicit THM-coupled MPM.

where $\boldsymbol{L}_{sp}^{k} = \sum_i \Delta \boldsymbol{v}_{si}^{k} \nabla S_{ip}$ is the velocity gradient, and $\Delta T_p^k = \sum_i \Delta T_i^k S_{ip}$ is the temperature increment.

(5) Update material point stresses $\boldsymbol{\sigma}'^{k+1}$ and other material point variables. In case of large deformation with large rotations, an objective stress rate, i.e., Jaumann stress rate, is utilized,

$$\boldsymbol{\sigma}_p'^{k+1} = \boldsymbol{\sigma}_p'^{k} + \boldsymbol{D} : \Delta\boldsymbol{\varepsilon}_p^{k+1} + \boldsymbol{\sigma}_p'^{k} \cdot \Delta\boldsymbol{\omega}_{sp}^{k+1} - \Delta\boldsymbol{\omega}_{sp}^{k+1} \cdot \boldsymbol{\sigma}_p'^{k} \tag{40}$$

where $\Delta\boldsymbol{\omega}_{sp}^{k+1} = \left[\boldsymbol{L}_{sp}^{k} - \left(\boldsymbol{L}_{sp}^{k}\right)^{T}\right] \Big/ 2$ is the spin tensor. The porosity and the volume of the material points can be updated using the total strain increment according to

$$n_{lp}^{k+1} = 1 - n_{lp}^{k} \Big/ \left(1 + \Delta\varepsilon_p^{k}\right), \qquad V_p^{k+1} = V_p^{k}\left(1 + \Delta\varepsilon_p^{k}\right) \tag{41}$$

where $\Delta\varepsilon_p^{k+1}$ is the trace of $\Delta\boldsymbol{\varepsilon}_p^{k+1}$. Furthermore, the intrinsic densities of the solid and the liquid can be updated according to Eq. (9) by explicit time stepping,

$$\rho_{sp}^{k+1} = \rho_{sp}^{k}\left(1 - \beta_s \Delta T_p^{k}\right), \qquad \rho_{lp}^{k+1} = \rho_{lp}^{k}\left(1 + \gamma_l \Delta p_p^{k} - \beta_l \Delta T_p^{k}\right) \tag{42}$$

Other temperature and/or pressure dependent properties can also be updated, such as the liquid viscosity and the specific heat capacity, though not considered in this study.

(6) Compute $\mathscr{E}^{int}$ and $\mathscr{E}^{ext}$ by Eq. (31), and calculate nodal temperature rate $\dot{T}_j^{k+1}$ by Eq. (30). Meanwhile, compute $\mathscr{M}_\alpha$, $\mathscr{F}_\alpha^{int}$, $\mathscr{F}_\alpha^{ext}$ and $\mathscr{F}^d$ according to Eq. (34), and calculate nodal intermediate velocities $\boldsymbol{v}_{\alpha j}^{*}$ by Eq. (33).

(7) Compute $\mathscr{L}$, $\mathscr{A}$, $\mathscr{B}$, and $\mathscr{N}_\alpha$ according to Eq. (36), and solve pressure Poison equation Eq. (35) for nodal incremental pore

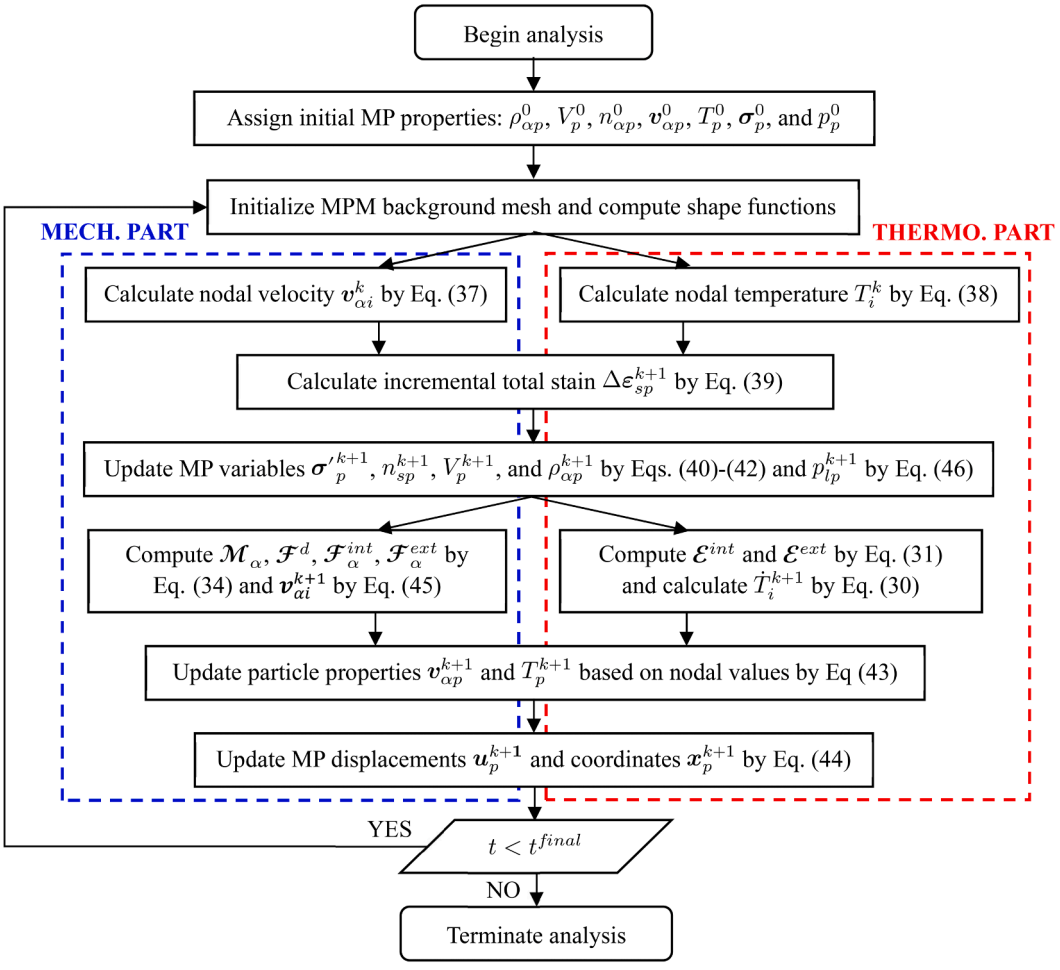


**Fig. 3.** Solution procedure of the fully explicit THM-coupled MPM.

pressure $\Delta p_j^{k+1}$.

(8) Compute the corrected nodal velocities $\boldsymbol{v}_{\alpha j}^{k+1}$ using $\Delta p_j^{k+1}$ by Eq. (33).

(9) Update particle primary variables, including velocities, temperature, and pore pressure, by extrapolating nodal information. In MPM, extrapolating incremental or total nodal values naturally results in two types of schemes: Particle-In-Cell (PIC) and Fluid-Implicit-Particles (FLIP). It is known that the former introduces excessive numerical dissipation for dynamic problems, and the latter has instability issues. A combined approach using mixed PIC and FLIP is proposed by Hammerquist and Nairn [75] as follows,

$$\psi_p^{k+1} = \alpha_\psi \sum_i \psi_i^{k+1} S_{ip} + (1-\alpha_\psi)\left(\psi_p^k + \sum_i \Delta\psi_i^{k+1} S_{ip}\right) \tag{43}$$

where $\psi$ represents different particle variables ($\psi = \boldsymbol{v}_\alpha, T, p$), and $\alpha_\psi$ is the PIC damping coefficient for $\psi$, ranging from 0 to 1. Eq. (43) can be reduced to the PIC method if $\alpha_\psi = 1$, and the FLIP method if $\alpha_\psi = 0$. Nairn and Guilkey [39] state that the PIC method for temperature updating suffers from numerical heat conduction, so it should not be adopted. The performance of the two schemes will be showcased in the following examples.

(10) Update particle displacements and coordinates by mid-point integration,

$$\boldsymbol{x}_p^{k+1} - \boldsymbol{x}_p^k = \boldsymbol{u}_p^{k+1} - \boldsymbol{u}_p^k = \Delta t \boldsymbol{v}_{sp}^k + \frac{1}{2}\sum_i \Delta \boldsymbol{v}_{si}^{k+1} S_{ip} \tag{44}$$

(11) If $t^{k+1} < t^{final}$, return to step (2) and enter the next loop; otherwise terminate the analysis.

Moreover, to facilitate the simulation of THM-coupled axisymmetric problems, we also present the main modifications of the fractional step-based formulations with regard to cylindrical coordinates. Details can be found in Appendix.

### 3.4.2. Explicit THM-coupled MPM

The solutions procedure for a fully explicit scheme is shown in Fig. 3. The main differences compared to the proposed semi-implicit MPM are as follows.

(1) The nodal velocities $\boldsymbol{v}_{\alpha i}^k$ are solved explicitly by,

$$\begin{cases} \mathscr{M}_s\left(\boldsymbol{v}_s^{k+1} - \boldsymbol{v}_s^k\right) + \mathscr{M}_l\left(\boldsymbol{v}_l^{k+1} - \boldsymbol{v}_l^k\right) = \mathscr{F}_m^{int} + \mathscr{F}_m^{ext} \\ \mathscr{M}_l\left(\boldsymbol{v}_l^{k+1} - \boldsymbol{v}_l^k\right) + \mathscr{F}^d\left(\boldsymbol{v}_l^k - \boldsymbol{v}_s^k\right) = \mathscr{F}_l^{int} + \mathscr{F}_l^{ext} \end{cases} \tag{45}$$

Here the lumped mass matrix is used for $\mathscr{M}_\alpha$ and $\mathscr{F}^d$ to facilitate explicit integration.

(2) The fluid is assumed to be weakly compressible, and the pore pressure is treated as a secondary variable which is directly calculated on particles based on the liquid compressibility,

$$p_p^{k+1} = p_p^k + \frac{\Delta t}{n_{lp}^{k+1}\gamma_l}\left(\beta_m \dot{\varepsilon}_{Tp}^{k+1} - n_{sp}^{k+1}\dot{\varepsilon}_{sp}^{k+1} - n_{lp}^{k+1}\dot{\varepsilon}_{lp}^{k+1}\right) \tag{46}$$

where $\dot{\varepsilon}_{Tp}^{k+1}$, $\dot{\varepsilon}_{sp}^{k+1}$, and $\dot{\varepsilon}_{lp}^{k+1}$ are the rate of thermal strain, solid volumetric strain of and liquid volumetric strain, respectively. Due to the explicit integration of pore pressure and drag force, the time step size is constrained also by the liquid compressibility and the permeability of the porous media (cf. [33,70]). To stabilize the pressure field in the explicit scheme, a simple pressure smoothing technique is used by interpolating particle pressure to nodes and re-interpolating to particles.

## 4. Numerical benchmarks

The numerical examples presented in this section are intended to validate and demonstrate the performance of the proposed THM-coupled MPM formulations in simulating different boundary value problems. The first two examples focus on the one-dimensional THM response in porous media, including the heating of a saturated half-space and the non-isothermal consolidation of a saturated soil column. The thermo-elastic response around a deeply buried heat source is further considered to demonstrate the robustness of the proposed method in simulating three-dimensional axisymmetric problems.

### 4.1. Heating of a saturated half-space

The first example considers a saturated semi-infinite space with its top surface subjected to a constant temperature load. This problem has been analytically solved by McTigue [76]. The geometry and boundary conditions of the problem are shown in Fig. 4. To simplify the problem, the half-space is modeled as a 1D saturated soil column which needs to be set sufficiently high to minimize the effect of wave reflection from the bottom boundary on the topsoil. The prescribed velocity boundary condition, where the bottom boundary is totally fixed and the side boundaries are fixed horizontally, is to ensure the 1D consolidation. The pore water is allowed to drain from the top surface only, while the other boundaries are impermeable. The soil domain is discretized into a column of cubic cells with a unique size of 0.2 m, and each cell is uniformly arranged with four material points. A constant temperature $T_1$ is applied instantaneously at the top boundary of the soil column at the start of the analysis. The soil column is modeled as a linear elastic

material. The convective heat transfer is not considered by McTigue [76] so does it in our case. The analytical solution for saturated porous media with incompressible constituents under drained conditions is expressed as,

$$T(h,t) = T_1\left[1 - \mathrm{erf}\left(\frac{h}{2\sqrt{\kappa t}}\right)\right] \tag{47a}$$

$$p(h,t) = \frac{bT_1}{1-c/\kappa}\left[\mathrm{erf}\left(\frac{h}{2\sqrt{ct}}\right) - \mathrm{erf}\left(\frac{h}{2\sqrt{\kappa t}}\right)\right] \tag{47b}$$

with $T(h,t)$ and $p(h,t)$ being the temperature and pore pressure at depth $h$ and time $t$, respectively, and the surface displacement $u_y(0,t)$ is given as,

$$u_y(0,t) = -\left[\frac{1-2\nu}{2G(1-\nu)}\frac{bT_1}{1+\sqrt{c/\kappa}} + \frac{1+\nu}{3(1-\nu)}\beta_s T_1\right]2\sqrt{\kappa t/\pi} \tag{47c}$$

where $\mathrm{erf}(*)$ is the error function, $T_1$ is the surface temperature, $\kappa = \kappa_m/C_m$ is the coefficient of thermal diffusivity, $c = kM/(\rho_l g)$ is the coefficient of consolidation, $b = 4G\beta_s/3 + Mn_l(\beta_l - \beta_s)$, $M = 2G(1-\nu)/(1-2\nu)$ is the P-wave modulus, $G$ is the shear modulus, and $\nu$ is the Poisson's ratio. Detailed solutions for displacement and stress can be found in Ref. [76].

In this example, the applied surface temperature $T_1 = 50$ °C, and the height of the soil column is set as 100 m. The material parameters are modified from [10], given as follows: Young's modulus $E = 6$ kPa, Poisson's ratio $\nu = 0.4$, porosity $n = 0.2$, specific heat $C_m = 167.2$ kJ kg$^{-1}$ °C$^{-1}$ (implemented by setting $\rho_s = \rho_l = 1000$kg m$^{-3}$ and $c_s = c_l = 167.2$ J kg$^{-1}$ °C$^{-1}$), thermal conductivity $\kappa_m = \kappa_s = \kappa_l = 836$ W m$^{-1}$ °C$^{-1}$, hydraulic conductivity $k = 4 \times 10^{-2}$ m s$^{-1}$, and volumetric thermal expansivity $\beta_s = \beta_l = 9 \times 10^{-7}$ °C$^{-1}$. The liquid compressibility is set as $\gamma_l = 1 \times 10^{-9}$ Pa$^{-1}$ for explicit MPM and weakly compressible semi-implicit MPM. As inequal $\beta_s$ and $\beta_l$ can be considered in the analytical solution, two additional cases with $\beta_l = 0$ and $\beta_l = 1.2 \times 10^{-6}$ °C$^{-1}$ are also benchmarked. Besides, the effect of information mapping strategies on the solution of temperature is investigated. The test conditions for all cases are summarized in Table 1. The time step size for the semi-implicit scheme is set as $8 \times 10^{-2}$ s. Due to the influence of liquid compressibility on the critical time step, the time step size for the explicit scheme needs to be much smaller which is set as $2 \times 10^{-4}$ s. All simulations are terminated at the simulated heating time up to $5 \times 10^4$ s.

Fig. 5 shows the time evolution of temperature, displacement, pore pressure, and effective stress at different soil depths. Both the numerical results by MPM and the analytical solutions are plotted in the same figure for comparison. As expected, the soil temperature gradually increases over time, leading to the expansion of soil and positive surface displacement. It is interesting that at the initial stage of heating, the temperature rise is not quite significant, while the pore pressure increases rapidly to its peak, at which the temperature is only about 5 °C. This phenomenon arises from the fact that the pore pressure is dependent on the rate of temperature and

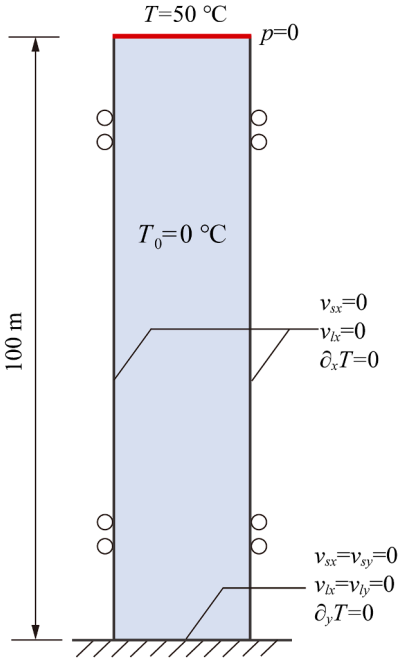


**Fig. 4.** Geometry and boundary conditions for 1D heating.

**Table 1**
Summary of the test conditions for all simulated cases in the 1D heating example.

| Case ID | Numerical scheme | Temperature mapping | Pressure smoothing | $\gamma_l$ [Pa$^{-1}$] | $\beta_l$ [°C$^{-1}$] |
|---|---|---|---|---|---|
| Semi - base | Semi-implicit | $\alpha_T = 0$ | No | 0 | 9E−7 |
| Semi - $\alpha_T = 1$ | Semi-implicit | $\alpha_T = 1$ | No | 0 | 9E−7 |
| Semi - $\gamma_l = 1$E−9 | Semi-implicit | $\alpha_T = 0$ | No | 1E−9 | 9E−7 |
| Semi - $\beta_l = 0$ | Semi-implicit | $\alpha_T = 0$ | No | 0 | 0 |
| Semi - $\beta_l = 1.2$E−6 | Semi-implicit | $\alpha_T = 0$ | No | 0 | 1.2E−6 |
| Explicit- base | Explicit | $\alpha_T = 0$ | Yes | 1E−9 | 9E−7 |
| Anal. - base | Analytical | – | – | – | 9E−7 |
| Anal.- $\beta_l = 0$ | Analytical | – | – | – | 0 |
| Anal.- $\beta_l = 1.2$E−6 | Analytical | – | – | – | 1.2E−6 |

deformation rather than their accumulative values, as indicated by the mass balance equation. Upon comparing the simulation results obtained from semi-implicit MPM with the analytical solutions, it is evident that the proposed method can achieve accurate and stable THM responses of porous media under thermal loading. The same observation holds independent of the choice of liquid expansivity $\beta_l$. It is notable that the magnitude of pore pressure is significantly affected by the value of $\beta_l$, indicating that it could generate unreasonable results if neglecting this factor during the THM coupling analysis.

By contrast, the simulation results by explicit MPM (not presented) are found to undergo severe pressure instabilities once the pressure smoothing is not applied. It is common in explicit hydrodynamics, as documented in the literature [34,35,42], not only because of the restriction of interpolation order but also the weakly compressible flow assumption that brings in wave propagation and reflection. In this work, adopting a simple pressure smoothing technique [33] renders the predictions of explicit MPM more stable

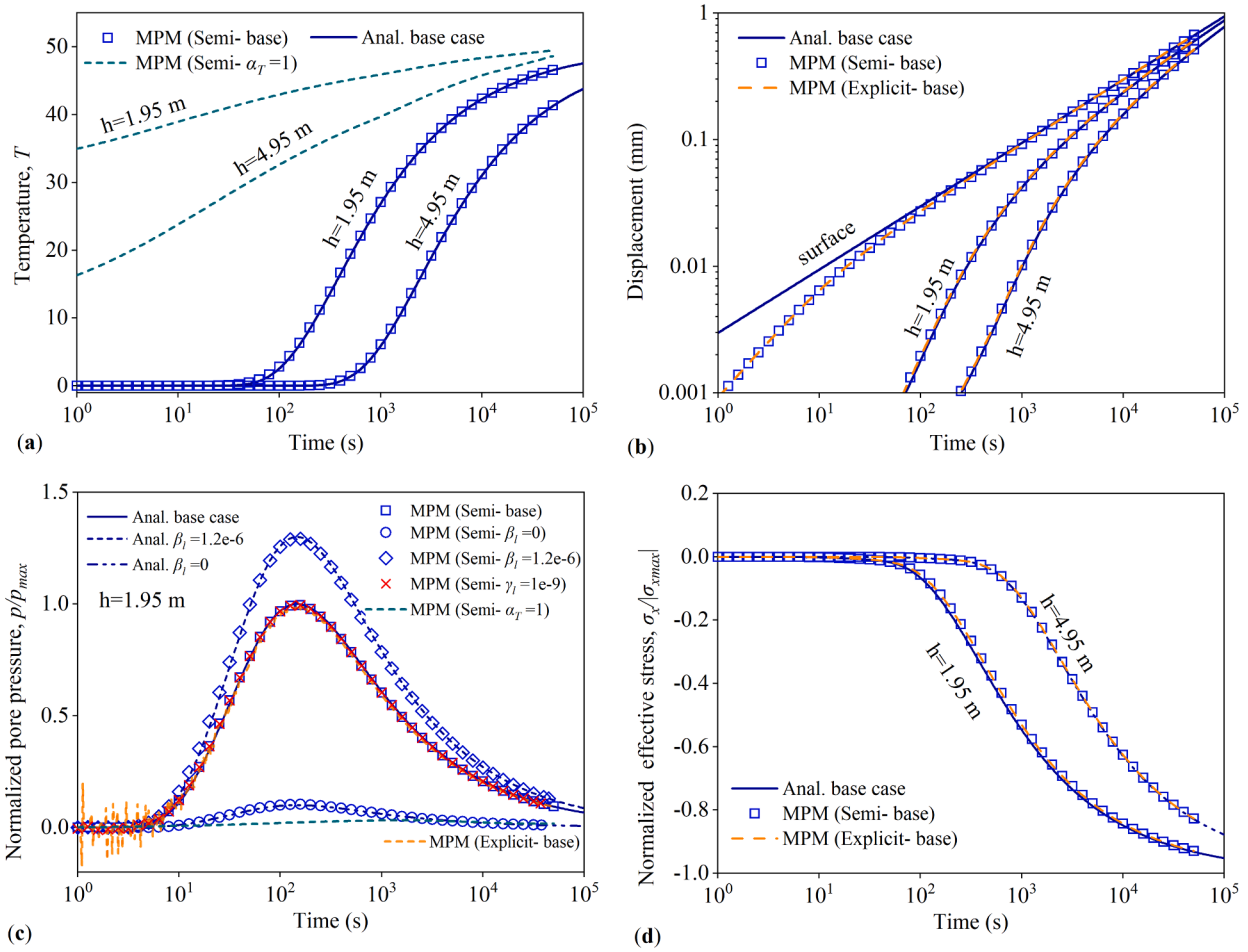


**Fig. 5.** MPM solutions against analytical solutions for the 1D heating of a saturated half-space: (a) temperature versus time, (b) surface displacement versus time, (c) normalized pore pressure $p/p_{max}$ versus time, in which $p_{max}$ is the maximum pore pressure in the base case, and (d) normalized effective stress $\sigma_x/|\sigma_{xmax}|$ versus time, in which $\sigma_{xmax}$ is the maximum lateral stress.

despite mild oscillations still observed during the initial stage of loading. It is worth noting that the pressure smoothing technique and other remedial measures, such as reduced integration or PIC damping method, cannot fundamentally address the pressure oscillation problem arising from the fluid incompressibility constraint. Moreover, the ensuing requirement of smaller time step sizes by such a technique renders it not as efficient as the fractional-step-based semi-implicit method. By contrast, the semi-implicit THM-coupled MPM shows a notable advantage in terms of both numeric accuracy and stability while offering acceptable efficiency.

Although the fluid compressibility may lead to unwelcome pressure oscillations, we sometimes require such dynamic features. This inspires the development of weakly compressible fractional step formulation in this work. From Fig. 5(c), it is evident that given a small value of liquid compressibility (see case "MPM(semi $\gamma_l = 1E{-}9$)"), the semi-implicit MPM based on weakly compressible fractional step formulation yields almost identical pore pressure as the case assuming incompressible fluid, indicating the correctness of the proposed formulation. The ability of the weakly compressible fractional step method to capture dynamic responses, such as the wave propagation in porous media caused by the instantaneous application of loads, is not shown due to limited space. Interested readers can refer to relevant literature by Jassim et al. [26] and Yuan et al. [44]. Another technical issue is concerned with the effect of different particle temperature mapping schemes on the resulting temperature field. Fig. 5(a) compares the particle temperatures updated by either incremental-based (i.e., $\alpha_T = 0$) or total-based (i.e., $\alpha_T = 1$) strategy. It is found that the obtained temperature using the latter strategy (see case "MPM(semi - $\alpha_T = 1$)") shows serious deviations compared to the actual solution. The deviations further cause spurious errors in the resulting displacement and pore pressure fields (see Fig. 5(b) and (c)). The observed discrepancy in temperature is attributable to what is referred to as numerical heat transfer [39]. Therefore, the total-based temperature mapping strategy is not advisable for advancing the solution of the temperature equation.

Fig. 6 further shows the primary variables versus soil depth in the semi-implicit base case. It is found the simulated results are stable in space and are all in excellent agreement with the analytical solution. This case demonstrates that the developed semi-implicit MPM is free of oscillations in both time and space despite using low-order interpolation functions. Overall, the proposed method can accurately consider a broad range of THM coupling effects while maintaining relatively high computational efficiency.

### 4.2. Non-isothermal consolidation

The second example revisits the problem of 1D non-isothermal consolidation of saturated soil. The example was initially designed by Aboustit et al. [77, 78]) and later adopted by other researchers such as Noorishad et al. [10], Lewis et al. [11], Cui et al. [17], Lei et al. [42], and Cui and Wong [18] to verify their FEM or MPM formulations and codes. The objective of this example is to evaluate the performance of the proposed THM-coupled formulations under combined thermal and mechanical loads. The geometry and boundary conditions are identical to the first example, except that the soil column is of a finite height of 7 m and is subjected to both a surface surcharge and a temperature load, as depicted in Fig. 7. The domain is discretized into 35 quadrilateral cells with a uniform size of 0.2 m, and each cell is arranged with four material points. The applied vertical surface traction $p_1$ and temperature $T_1$ are 1 Pa and 50 °C,

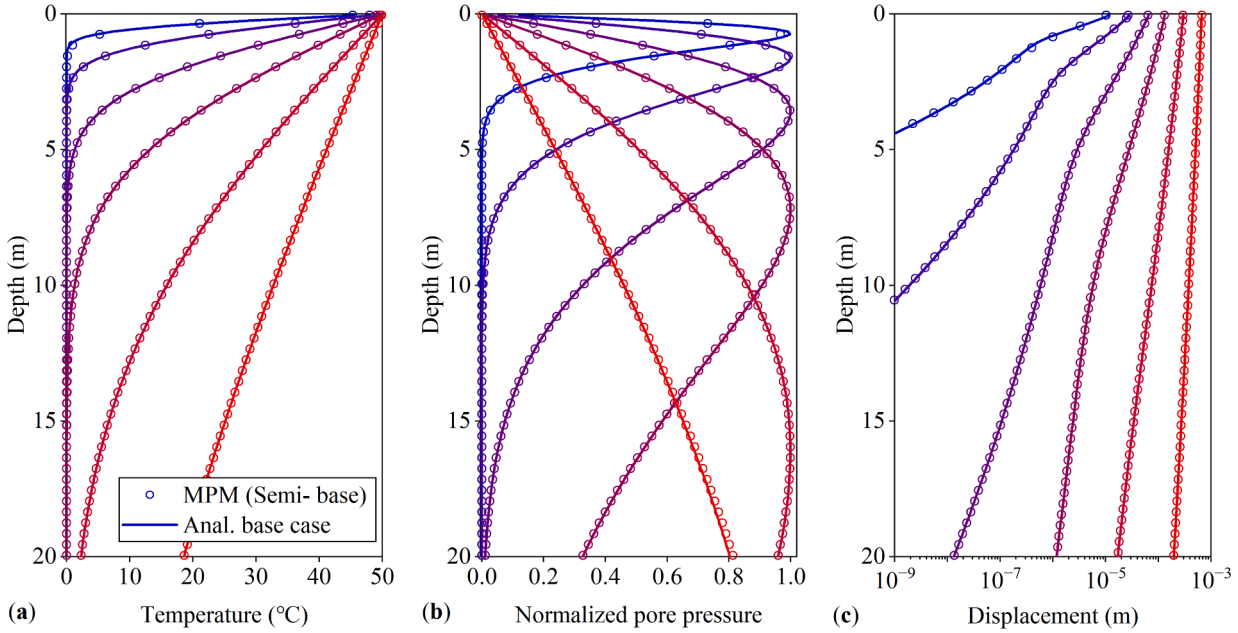


**Fig. 6.** Spatial distributions of (a) temperature, (b) pore pressure, and (c) displacement at different time instances: $t$ = 20 s, 100 s, 500 s, 2000 s, 10 000 s, and 50 000 s, represented by lines from up (blue) to bottom (red), respectively. (For interpretation of the references to color in this figure legend, the reader is referred to the web version of this article.)

respectively. For comparative purposes, cases with prescribed temperature or prescribed traction only are also performed. The three parallel cases are labeled as Case 1 ($p_1 = 1\,\text{Pa}, T_1 = 50\ \ ^\circ\text{C}$), Case 2 ($p_1 = 1\,\text{Pa}, T_1 = 0\ \ ^\circ\text{C}$), and Case 3 ($p_1 = 0\,\text{Pa}, T_1 = 50\ \ ^\circ\text{C}$). The soil is modeled as a linear elastic granular material with the same material parameters presented in the previous example. The time step sizes for semi-implicit and explicit schemes are set as $8 \times 10^{-2}$ s and $1 \times 10^{-4}$ s, respectively.

Fig. 8 displays the temperature evolution at the depths of 1 m, 3 m, and 5 m. Fig. 8(a) shows that the temperature gradually increases over time and eventually approaches 50 °C. The simulated temperatures by MPM at the depths of 3 m and 5 m match well with the predictions by Lewis et al. [11], while a minor discrepancy at the depth of 1 m is observed in the initial stage of the analysis. The discrepancy is also reported by Cui et al. [17] in their FEM analysis compared to Lewis et al. [11], whereas their results are consistent with ours. The deviation may be because Lewis et al. employ relatively larger time step intervals in their simulation (10 s per step after a simulation duration of 1.1 s).

Fig. 9 displays the pore pressure evolution at the depths of 1 m and 3 m. Again, the result obtained by the explicit MPM is treated by pressure smoothing. In Case 2 (the isothermal case), the pore pressure initially equals the applied boundary traction and gradually decreases to zero over time. This indicates that the surcharge load is initially borne entirely by the pore water during consolidation and subsequently transferred onto the soil skeleton as the pore water drains away. Due to a shorter drainage path, the topsoil layer (e.g., $h = 1$ m) dissipates pore pressure faster than those farther away from the surface (e.g., $h = 3$ m). Case 3 involves thermal loading only, in which the pore pressure shows similar trends as that of the case in Section 4.1, except that the peak value, affected by the fixed bottom boundary, varies with the depth of soil (see the top-right subfigure in Fig. 9). Case 1 is simulated with combined thermal and mechanical loadings. However, since the thermal-induced pressure does not play a dominant role in this scenario (the peak pressure is observed to be no larger than 1% that of the surface surcharge), the resulting pore pressure nearly overlaps with that of the isothermal case. Overall, the pore pressure data, obtained from either the semi-implicit MPM or smoothed explicit MPM, are in good agreement with the FEM work by Lewis et al. [11] and Cui et al. [17].

Fig. 10 further shows the consolidation (surface displacement) curves for both the isothermal and non-isothermal cases. A notable feature in Case 1 is the nonmonotonic consolidation behavior of soil changed from subsidence to expansion. This behavior is a characteristic of non-isothermal consolidation and is determined by the consolidation coefficient $c$ ($= kM/\mu$) and the thermal diffusivity $\kappa$ ($= \kappa_m/C_m$). The two factors control the rate at which the consolidation process proceeds and the rate of heat transfer of soil from the hot end to the cold end, respectively [79]. In this case, $c$ ($= 5.24 \times 10^{-2}$) is about ten times greater than $\kappa\left(= 5 \times 10^{-3}\right)$, indicating that the rate of heat transfer or, deductively, the rate of expansion of soil, is slower than the rate of consolidation. This is responsible for the out-of-sync behavior observed in the pore pressure curves of Case 2 and Case 3. If given different properties of $c$ and $\kappa$ and different boundary conditions, the soil may exhibit different consolidation behaviors, from monotonic to nonmonotonic and cyclic responses [80,81]. The simulated displacements for all three cases demonstrate good agreement with FEM results, except that the maximum displacement differs slightly from the result of Lewis et al. [11]. This discrepancy may be attributed to their simplification of the thermal coupling term $\beta_m \dot{T}$ in the mass balance equation, which can lead to an overestimation in the rate of pore pressure

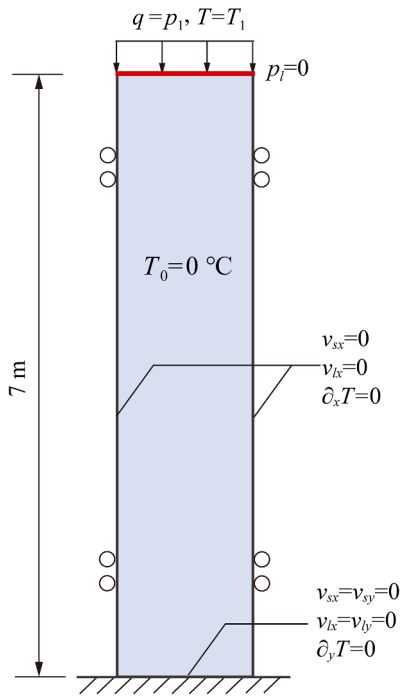


**Fig. 7.** Geometry and boundary conditions for non-isothermal consolidation.

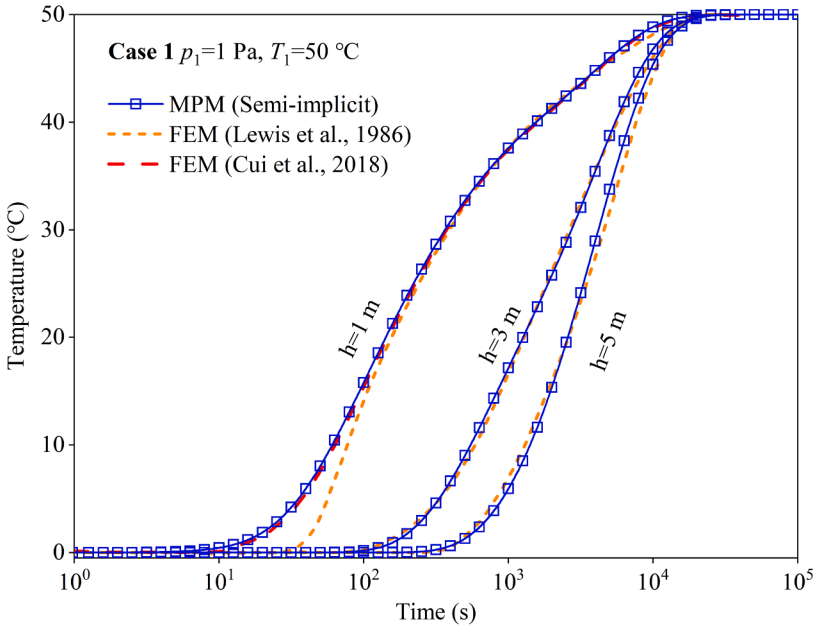


**Fig. 8.** Temperature versus time at the depths of 1 m, 3 m, and 5 m.

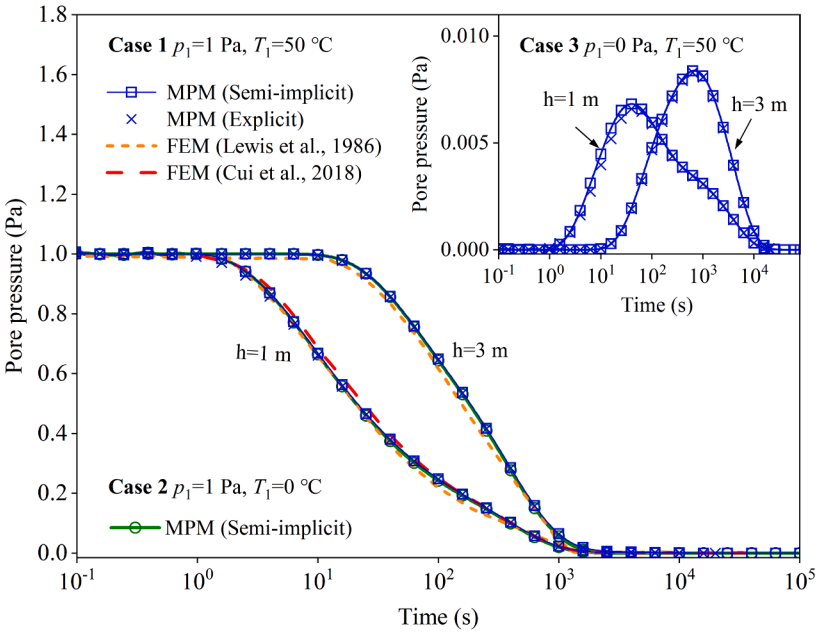


**Fig. 9.** Pore pressure versus time at the depths of 1 m and 3 m.

dissipation. Like our approach, Cui et al. [17] also took the thermal coupling effect into consideration, and their outcomes are in excellent agreement with ours. To sum up, the proposed MPM formulations can effectively model the coupled THM responses of porous media under diverse boundary conditions.

### 4.3. *THM response around a point heat source*

The following example involves the thermoelastic response around a deeply buried point heat source, a classical problem frequently used to benchmark the THM-coupled FEM codes. This problem was solved analytically by Booker and Savvidou [82] and

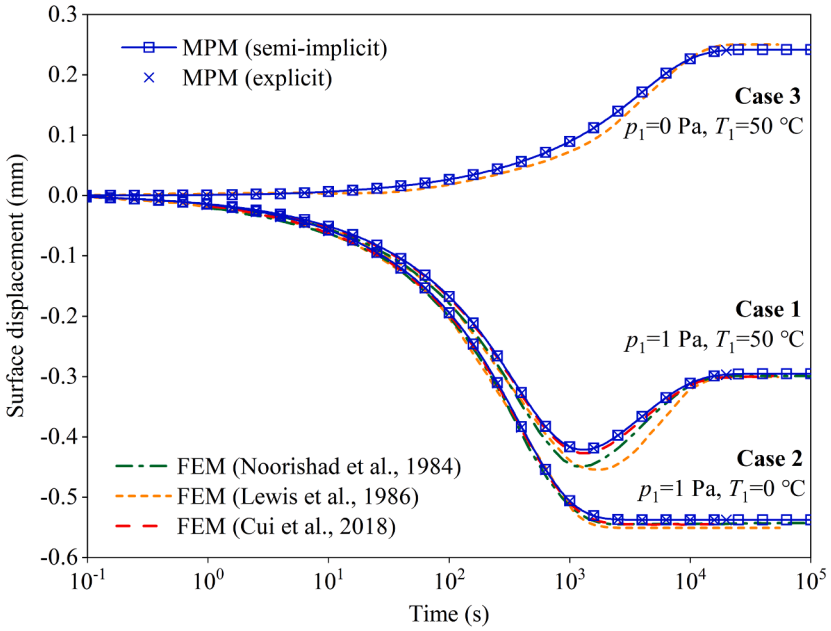


**Fig. 10.** Surface settlement versus time for both non-isothermal and isothermal conditions.

more recently corrected by Chaudhry et al. [83] with regard to the stress part of the analytical solution. The point heat source problem is a typical axisymmetric problem and is preferable to be solved in cylindrical coordinates. In this section, both 3D and axisymmetric MPM analyses are presented to demonstrate the robustness of the semi-implicit THM-coupled MPM. Explicit MPM is not used for this example due to its low efficiency.

Fig. 11 shows the MPM model setup for 3D and axisymmetric analyses. For the 3D case, a 1/8 region of the entire space is simulated, considering the problem space is symmetric. The applied point heat source is located at the origin of the coordinate system. As the focus is the soil behavior around the heat source, it requires minimizing the effect of outer boundaries by simulating a relatively large domain with fine mesh sizes. After several tests, it was found that 10 m in each dimension with an element size growing from $10^{-2}$ to 2.5 m is enough to weaken the boundary effect. The use of increasing meshing size helps capture more accurate results near the heat source and, meanwhile, does not significantly increase the computation intensity. The modeling domain is then divided into 8000 quadrilateral elements, each containing eight material points initially. A total number of 64 000 material points is simulated in the 3D case. In the axisymmetric case, the domain is divided into 400 rectangular elements, with four material points in each cell and totaling 1600 material points. This could significantly reduce the computational cost compared to the 3D case. The prescribed boundary conditions require the normal displacements of both the liquid and the solid phases to be constrained to zero along the inner boundary, while at the outer boundary, the temperature and the pore water pressure remain unchanged throughout the simulation, i.e., $T_0 = 0$ °C and $p_0 = 0$Pa. A point heat source of $Q_h = 1000$ W is applied to propagate the transfer of heat. Some cautions should be taken for the axisymmetric case. First, nodes at the rotationally axisymmetric boundary ($r = 0$) should be strictly constrained in the normal direction. Second, the input of the heat source should be in power per radian, which is $125/2\pi$ W in this case. Furthermore, the assignment of traction along the outer boundaries should be in force per radian and properly dependent on position, although this is not relevant to our case [39].

The soil is modeled as a linear elastic material with the following material properties: Young's modulus $E = 5 \times 10^3$Pa, Poisson's ratio $\nu = 0.3$, porosity $n = 0.16$, solid density $\rho_s = 2290$kg m$^{-3}$, liquid density $\rho_l = 1000$kg m$^{-3}$, solid specific heat capacity $c_s = 918$ J kg$^{-1}$ °C$^{-1}$, liquid specific heat capacity $c_l = 4280$ J kg$^{-1}$ °C$^{-1}$, solid thermal expansivity $\beta_s = 1.5 \times 10^{-5}$ °C$^{-1}$, liquid thermal expansivity $\beta_l = 4 \times 10^{-4}$ °C$^{-1}$, solid thermal conductivity $\kappa_s = 1838$ W m$^{-1}$ °C$^{-1}$, liquid thermal conductivity $\kappa_s = 600$ W m$^{-1}$ °C$^{-1}$, and hydraulic conductivity $k = 2 \times 10^{-4}$ m s$^{-1}$. The analytical solution is given as follows,

$$T(\rho,t) = \frac{Q}{4\pi\kappa_m\rho}\left[1 - \mathrm{erf}\left(\frac{h}{2\sqrt{ct}}\right)\right] \tag{48a}$$

$$p(\rho,t) = \frac{bQ}{4\pi\kappa_m\rho(1-c/\kappa)}\left[\mathrm{erf}\left(\frac{h}{2\sqrt{ct}}\right) - \mathrm{erf}\left(\frac{h}{2\sqrt{\kappa t}}\right)\right] \tag{48b}$$

where $T(\rho,t)$ and $p(r,t)$ are the temperature and pore pressure at time $t$ and distance $\rho$ with $\rho = \sqrt{x_1^2 + x_2^2 + x_3^2}$, $Q$ is the heat source,

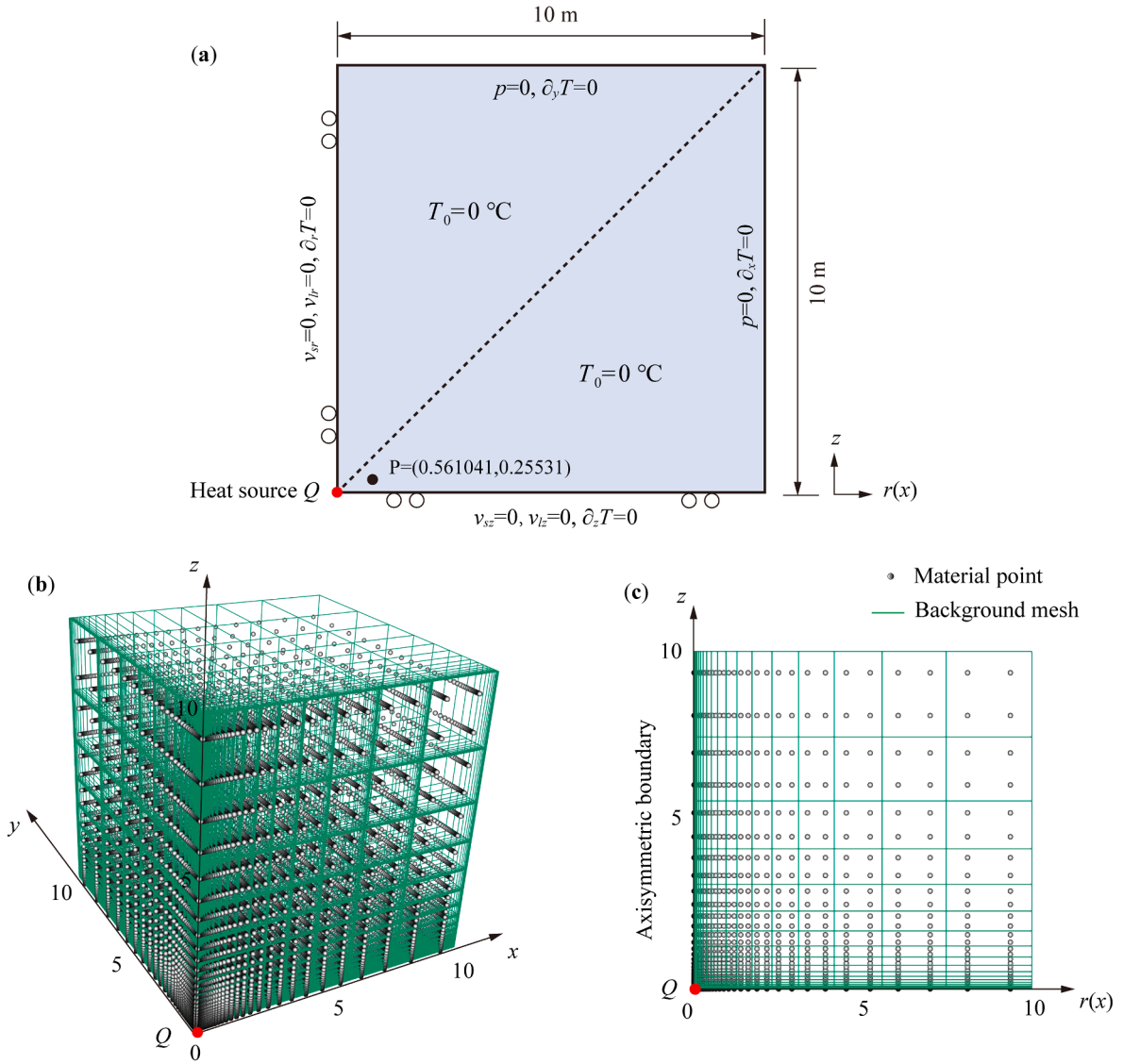


**Fig. 11.** Model setups for (a) 3D and (b) axisymmetric analyses of the THM response around a deeply buried point heat source.

and other parameters are the same as Eq. (47). The solution for displacement and effective stress can be referred to Chaudhry et al. [83].

Figs. 12 and 13 show the contour results of the 3D case and the axisymmetric case, respectively. To display the results more clearly, we post-treat the solution in the axisymmetric case by Delaunay triangulation. It is found both cases show nearly identical solutions. The resulting temperature displays a perfect circular distribution around the point heat source, which is a natural outcome of isotropic heat transfer in a symmetrical configuration. The same feature is observed in pore pressure and displacement magnitude since the hydraulic and mechanical responses solely arise from the thermal variation. However, differing from the temperature that changes monotonously in the radial direction, the pore pressure and the displacement show a peak value, and the peak shifts away from the heat source over time. Besides, in the axisymmetric case, the radial displacement $u_r$ is bilaterally symmetric with the axial displacement $u_z$ with respect to the 45-degree line, indicating the correctness of the axisymmetric formulation. Overall, both results in 3D and axisymmetric cases demonstrate reasonable spatial distribution and time evolution of the primary variables at a qualitative level. Quantitive verifications of the numerical results are performed later by comparing them with analytical results.

Fig. 14 presents the MPM results against the analytical solutions as a function of time at an arbitrarily chosen point $P(0.561041\ \text{m}, 0.25531\ \text{m}, 0\ \text{m})$. It is found that the evolutions of the four fields in both the axisymmetric and 3D cases are in good agreement with the analytical solutions. Slight pressure oscillation at the initial stage of the simulation and minor deviations in stress components are observed. The deviations in stress components are probably attributed to the fact that the MPM uses material points instead of Gaussian points for stress integration. Fig. 15 further compares the spatial distribution of the axisymmetric results along the

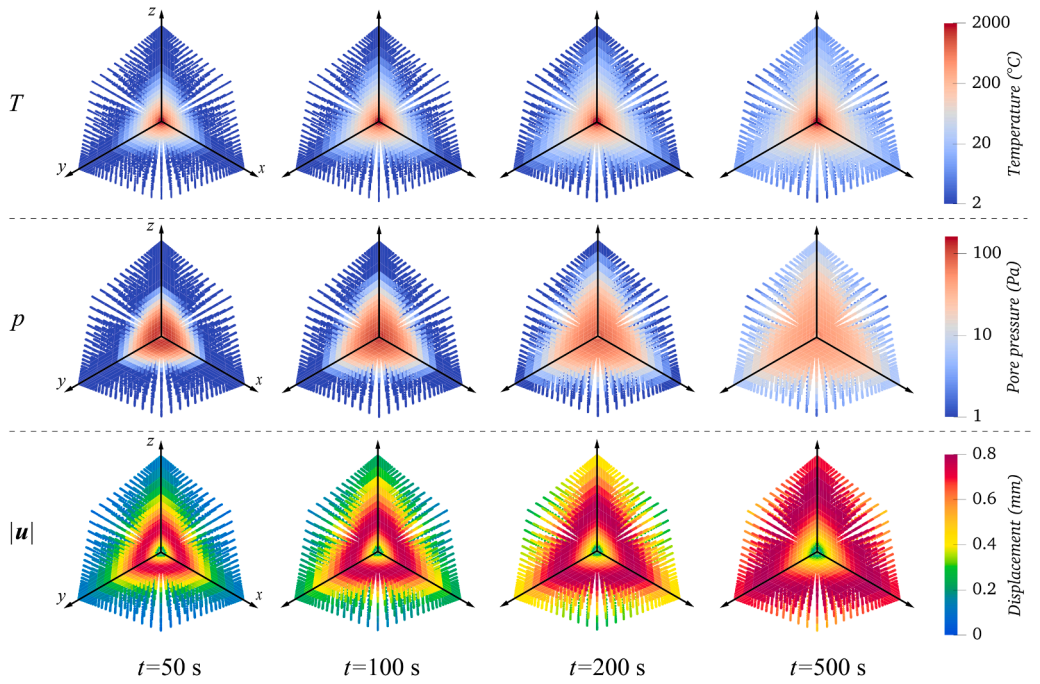


**Fig. 12.** Contour results of temperature, pore pressure, and displacement magnitude $|\boldsymbol{u}|$ within 1 m around the point heat source in the 3D case.

45-degree line at the time of 100 s. The major numerical errors are found in the region near the heat source. However, by using a finer mesh, for example, one in which the element size is half of that of the reference case (denoted as coarser mesh case), the accuracy of the simulation results can be improved, as indicated by the green lines in Fig. 15. It is also worth noting that the simulated heat source problem is a so-called singularity problem which means some variables, e.g., temperature and stresses, approach infinite when $r$ and $z$ tend to zero. That is why the simulation results near the heat source are not as good as those far away, even in the finer mesh case. The fluctuation observed in stress distribution is also a result of the inaccurate stress integration in low-order elements, which can be minimized by further employing stress or strain smoothing techniques, e.g., $\overline{B}$ and $\overline{F}$ method (cf. [84]). Overall, the developed coupled MPM can correctly simulate the 3D and axisymmetric problems involving multiphysics coupling.

## 5. Application example: THM analysis of a slope

Granular soils with ice-like cementation, such as frozen soils and gas hydrate-bearing sediments, are susceptible to changes in temperature [2,85]. For instance, the rising temperature may cause the melting and gasification of the ice-like bond and lead to the weakening or softening of the bearing soils [86–88]. This example focuses on the thermal response and failure of a thermally sensitive slope caused by temperature change. For simplification, the effect of temperature change on the material responses is incorporated into the soil constitutive models and the phase transition is not considered in the conservation equations. Further development of the method relevant to phase change problems will be conducted in the future.

Fig. 16 depicts the geometry and boundary conditions of the saturated slope under consideration. The bottom boundary is rigidly fixed, and the left and right are roller boundaries. The top boundaries are free and drained. To further demonstrate the capability of the proposed approach in tackling diverse initial and boundary value problems, three typical geotechnical problems are simulated, including the self-weight consolidation, the THM response due to heating, and the slope slide triggered by temperature rise. The temperature boundary illustrated in the figure is set only for the latter two problems. The linear elastic model is used in the first two problems, and for the final problem, a thermal- and strain-softening Mohr–Coulomb model is adopted to capture the motion of the slope.

### 5.1. Self-weight consolidation

It is preferable to generate a stable in-situ stress field through self-weight consolidation before we proceed to the latter slope failure case [9,33]. The gravitational acceleration is taken as 9.81 $\mathrm{m\,s^{-2}}$. The material properties are given as follows: Young's modulus $E = 2 \times 10^7$Pa, Poisson's ratio $\nu = 0.3$, porosity $n = 0.2$, intrinsic density of solid grains $\rho_s = 2600\mathrm{kg\,m^{-3}}$, intrinsic density of liquid $\rho_l = 1000\mathrm{kg\,m^{-3}}$, and hydraulic conductivity $k = 1 \times 10^{-8}$ $\mathrm{m\,s^{-1}}$. To accelerate the seepage process, the hydraulic conductivity is

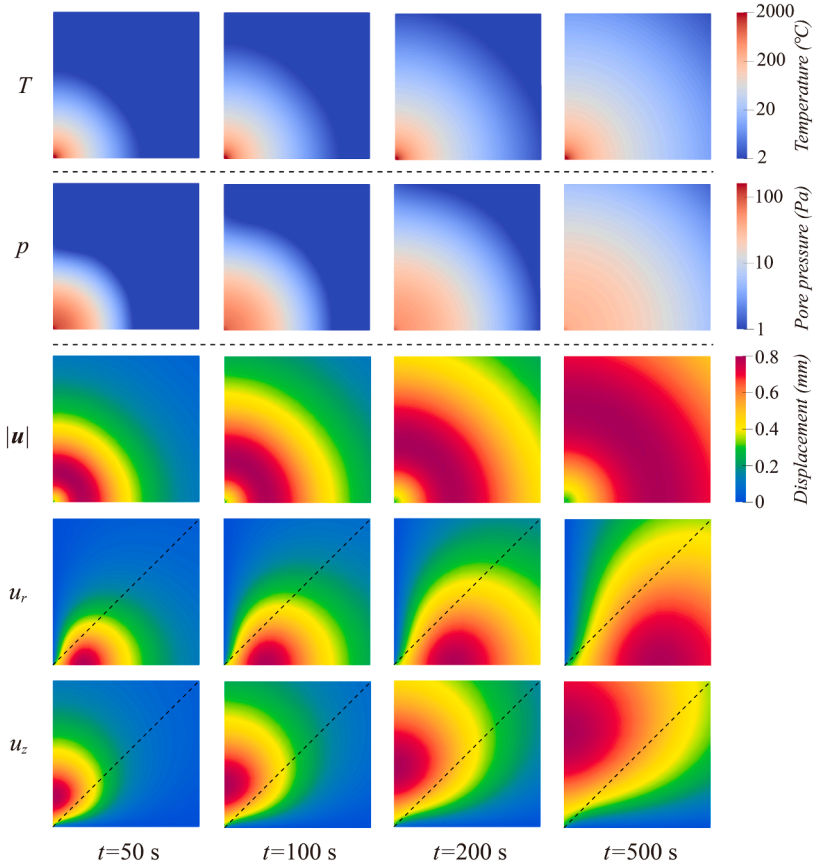


**Fig. 13.** Contour results of temperature, pore pressure, displacement magnitude $|\boldsymbol{u}|$, radial displacement $u_r$, and axial displacement $u_z$ within 1 m around the point heat source.

amplified by a factor of 86400 s/day, making the simulation time of 1 s equivalent to the seepage duration of 1 day. The time increments are chosen as $1 \times 10^{-3}$ s and $2 \times 10^{-5}$ s for semi-implicit and explicit MPM, respectively. It is observed the solutions exhibit periodical oscillations for both semi-implicit and explicit methods. This is a natural outcome of the instantaneous application of gravity on elastic media. To mitigate this issue, an artificial damping $\left(=-\alpha_{damp}\boldsymbol{v}_{\alpha}\right)$ is added to the particle acceleration in each time step, with a damping factor $\alpha_{damp} = 5/\text{s}$ [28,42].

Figs. 17 and 18 present the contour plots of pore pressure and displacement fields solved by two methods with and without damping. Five points, i.e., A (0 m, 0 m), B (10 m, 0 m), C (5 m, 5 m), D (14 m, 4 m), and E (8 m, 10 m), are chosen to analyze the evolution of pore pressure and displacement qualitatively. The numerical results of the chosen points are shown in Fig. 19. As the two methods generate nearly identical simulation results, only the result for semi-implicit MPM is presented. It can be observed that without damping, the numerical oscillations in pressure and displacement could also shrink with time but at a rather low speed. However, with a damping of 5/s adopted, the oscillations are rapidly reduced. Despite the use of particle damping, the same state is obtained at the final stable stage of the consolidation as that of the non-damped case. The final stabilized state of consolidation will serve as the initial conditions of the slope failure problem in Section 5.3.

### 5.2. Thermal transfer analysis

Thermal transfer underpins many engineering applications, such as thermal piles and the heating of wellbores by hot water injection [1,89]. The latter is also one of the main approaches to dissociating gas hydrate. In this case, we consider a vertical wellbore near the slope, where hot water is injected to heat the wellbore. The temperature of the injected water, denoted as $T_1$, is kept constant at 50 °C. The height of the wellbore is 6 m, and the radial size of the borehole is neglected. The initial–boundary value problem can be simplified as shown in Fig. 16. The initial temperature is set as 0 °C, and the temperature of the inner boundaries remains unchanged during the heating process. The slope is modeled with the same material as the previous section. The thermal-related material properties are given as follows: specific heat capacity of solid $c_s = 837$ J kg$^{-1}$ °C$^{-1}$, specific heat capacity of liquid $c_l = 4186$ J kg$^{-1}$ °C$^{-1}$, volumetric thermal expansion coefficient of solid $\beta_s = 3 \times 10^{-5}$ °C$^{-1}$, volumetric thermal expansion coefficient of

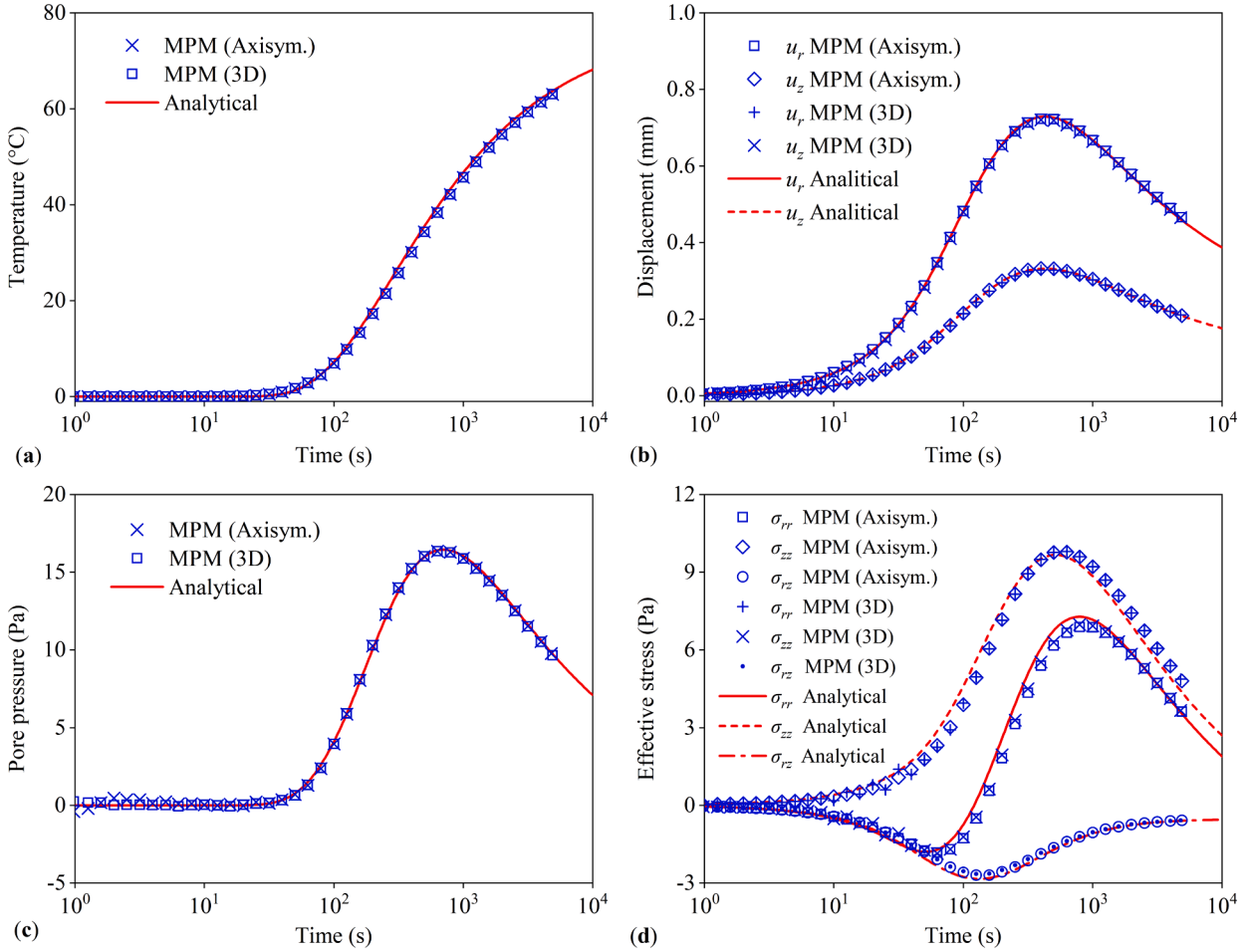


**Fig. 14.** MPM results against analytical solutions: (a) temperature, (b) displacement components $u_r$ and $u_z$, (c) pore pressure, and (d) effective stress components $\sigma_{rr}$, $\sigma_{zz}$, and $\sigma_{rz}$ as a function of time at point (0.561041 m, 0.25531 m, 0 m).

liquid $\beta_l = 2.1 \times 10^{-4}\,^{\circ}\mathrm{C}^{-1}$, thermal conductivity coefficient of solid $\kappa_s = 1.838$ W m$^{-1}$ °C$^{-1}$, thermal conductivity coefficient of liquid $\kappa_s = 0.6$ W m$^{-1}$ °C$^{-1}$. Again, to accelerate the thermal transfer and pore pressure dissipation, both the thermal conductivity and permeability coefficients are amplified by 86400 s/day. Similar treatments have been adopted by Lei et al. [42] and Zhao et al. [88].

Fig. 20 shows the contour plots of temperature and excess pore pressure for explicit and semi-implicit methods. It is observed that both methods give similar pore pressure distributions. At the initial stage of the heating process, the expansion of solid and water results in a rapid increase of excess pore pressure around the heating region. With the drainage of pore water, the excess pore pressure starts to dissipate after reaching its peak. Given a lower permeability, it exhibits a higher peak value and a slower rate of dissipation. The thermo-hydraulic responses of the slope during the heating process show the same trend as the previous one-dimensional example (see Section 4.1). Fig. 21 shows the contour plots of displacement components in both the $x$ and $y$ directions. It is observed that during the early stage of the heating process, the slope deforms toward the free sides in both lateral and vertical directions, exhibiting an expansive behavior. However, with the heating process continuing, the behavior of the slope changes from expansion to contraction, with a trend to reach a stable state. Again, this is attributed to the coupling effect of thermo-hydromechanics. Overall, the solutions of temperature, excess pore pressure, and displacement show very smooth spatial distributions, indicating that the proposed method can capture reasonable and stable THM responses for engineering-scale problems.

### 5.3. Slope failure caused by temperature rise

In engineering failure analysis, the contribution of purely thermal deformation is often negligible compared to temperature-induced material degradation. For instance, several studies have demonstrated that an increase in temperature leads to a decrease in cohesion and friction angle of ice- or hydrate-bonded soils as a result of the loss of ice/hydrate bond [2,87,90]. In this example, we

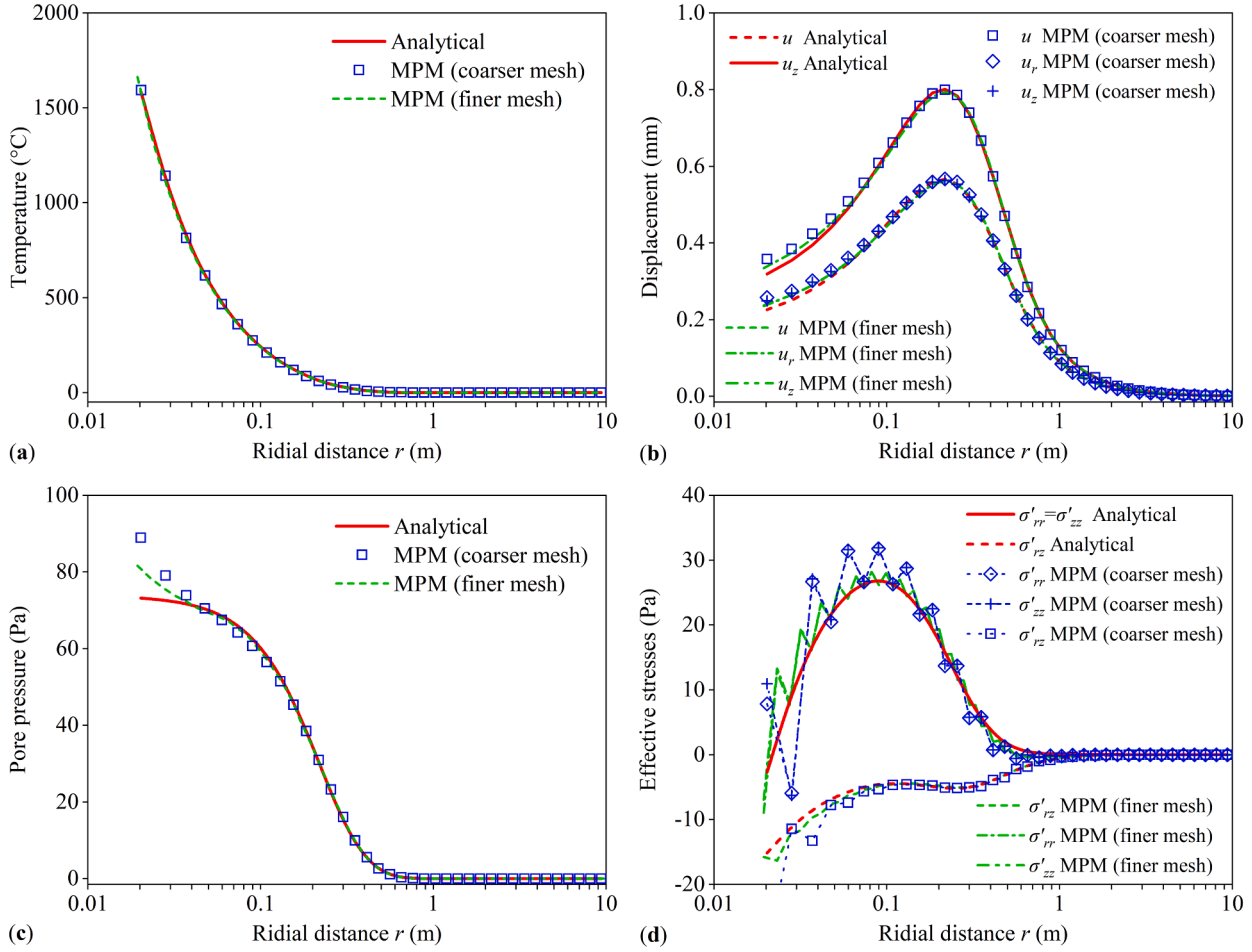


**Fig. 15.** Spatial distribution of (a) temperature, (b) displacement components $u_r$ and $u_z$, (c) pore pressure, (d) effective stress components $\sigma_{rr}$, $\sigma_{zz}$, and $\sigma_{rz}$ along the 45-degree line at $t = 100$ s. (For interpretation of the references to color in this figure legend, the reader is referred to the web version of this article.)

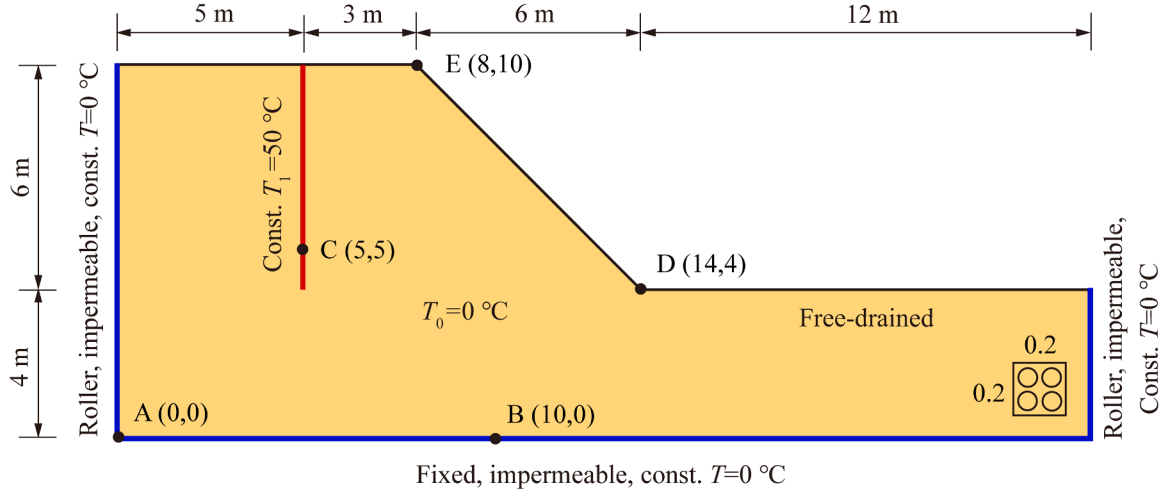


**Fig. 16.** Geometry and boundary conditions for the saturated slope.

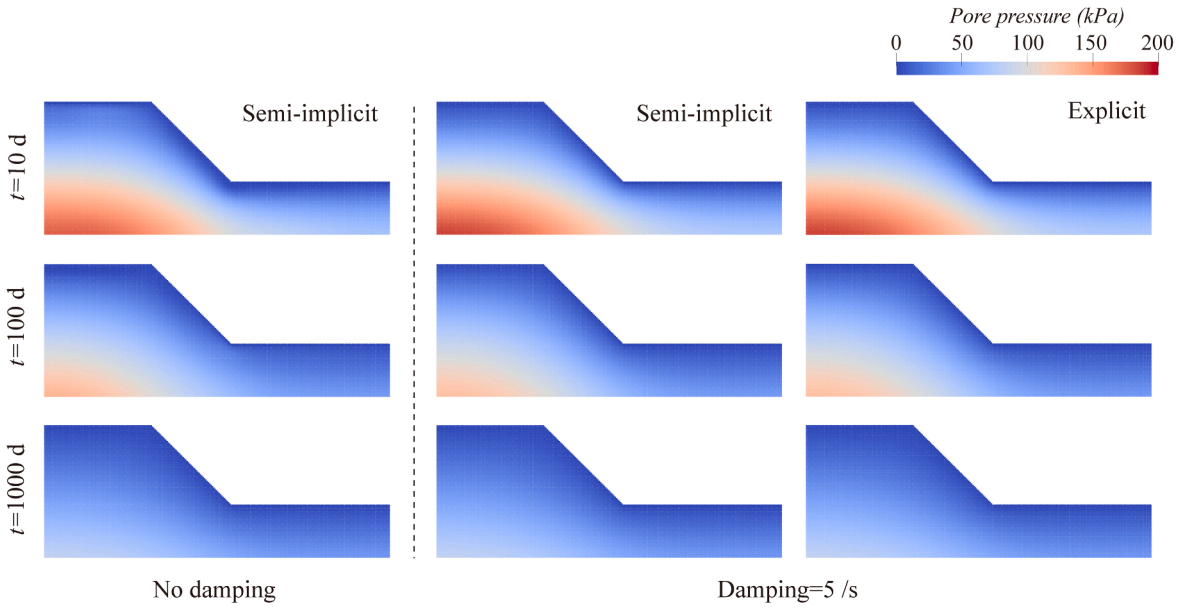


**Fig. 17.** Comparison of the pore pressure field for semi-implicit MPM and explicit MPM with and without damping at different time instances during the gravity loading.

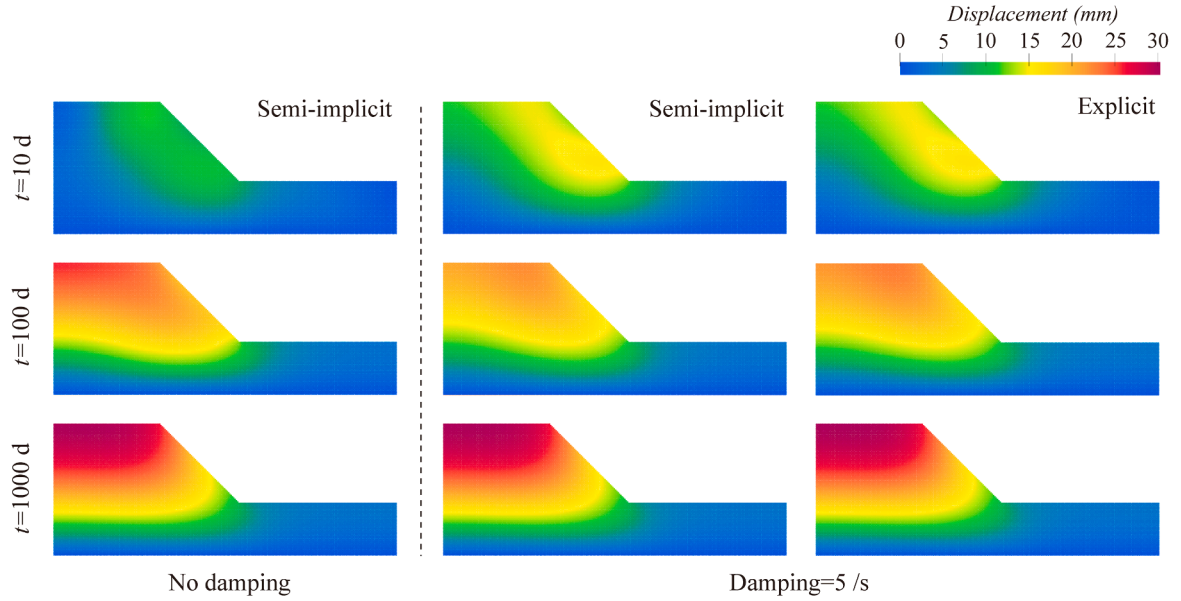


**Fig. 18.** Comparison of the displacement field for semi-implicit MPM and explicit MPM with and without damping at different time instances during the gravity loading.

adopt a non-associated elastoplastic Mohr–Coulomb model proposed by Monterey and Willam [91] and widely used in previous MPM studies (cf. [33,92]). The soil's softening behavior caused by temperature rise and strain accumulations is considered by incorporating a softening model modified from [8,93], in which the effective cohesion $c^{'}$ and effective friction angle $\varphi^{'}$ decrease exponentially with temperature $T$ and plastic deviatoric strain $\varepsilon_p^d$ as follows,

$$c^{'} = c^{'}_{res} + \left(c^{'}_0 - c^{'}_{res}\right) exp\Big( - \eta\varepsilon_p^d - \eta_T(T - T_0)\Big) \tag{49a}$$

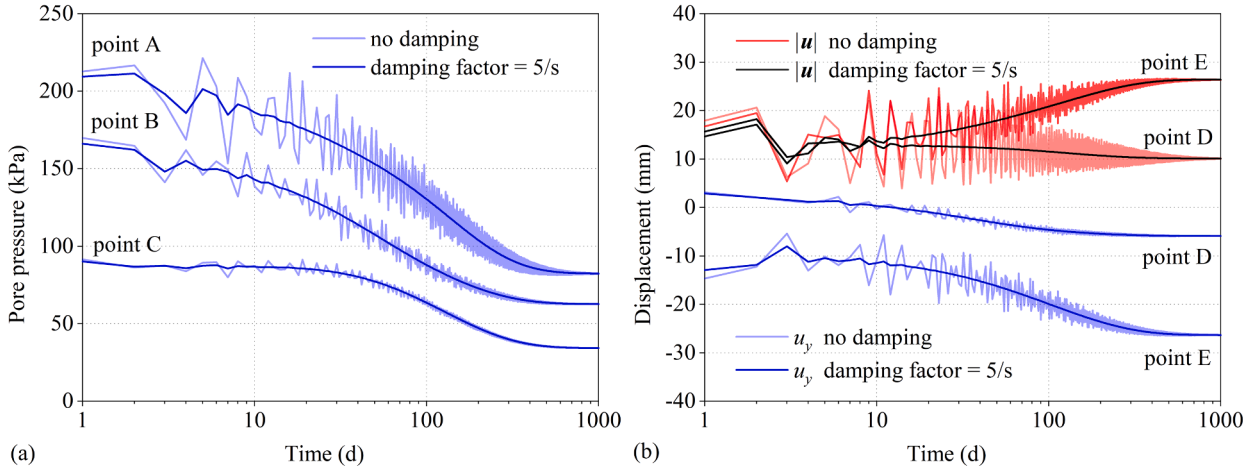


**Fig. 19.** Time evolution of (a) pore pressure at points A, B, and C, and (b) displacement at points D and E for semi-implicit THM-coupled MPM.

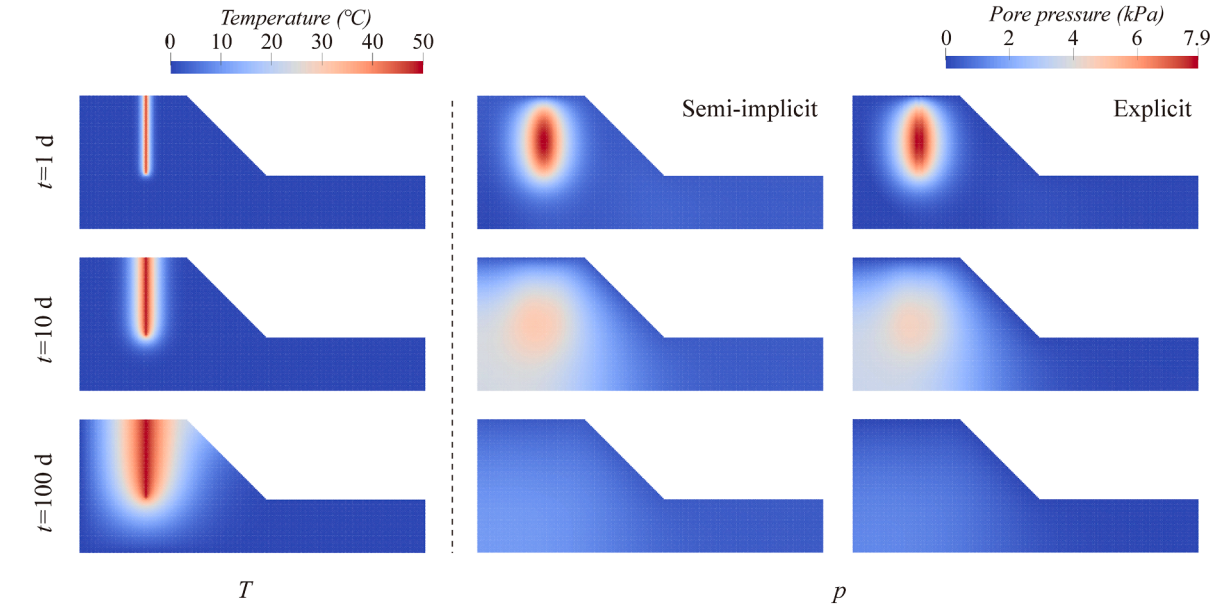


**Fig. 20.** Temperature and pore pressure fields at different time instances during the heating process for both the semi-implicit and explicit MPM.

$$\varphi' = \varphi'_{res} + (\varphi'_0 - \varphi'_{res}) exp\Big( - \eta \varepsilon_p^d - \eta_T (T - T_0) \Big) \tag{49b}$$

where $c'_0$ and $\varphi'_0$ are the effective cohesion and the effective friction angle at the reference temperature $T_0$, $c'_{res}$ and $\varphi'_{res}$ are the residual values of $c'$ and $\varphi'$, and $\eta$ and $\eta_T$ are the shape coefficients which control the strain softening and thermal softening. In this example, the material properties used are given as follows: $c'_0 = 20$ kPa, $c'_{res} = 1$ kPa, $\varphi'_0 = 27°$, $\varphi'_{res} = 15°$, $\eta = 100$, $\eta_T = 1$, and $T_0 = 0$ °C. Other elastic material properties and thermal properties are the same as in the previous sections. The boundary conditions are the same as in Section 5.2. The stable state after consolidation in Section 5.1 is chosen as the initial condition of the simulation.

Figs. 22 and 23 present the numerical results obtained from the semi-implicit MPM and the explicit MPM, respectively. Both methods show highly similar simulation outcomes. The failure mechanism of the slope can be explained as follows. As the temperature increases, the cohesion and friction of the soil decline, resulting in the soil adjacent to the heat source yielding and forming a vertical shear band. With further temperature rise, the shear band extends downwards, creating a visible circular sliding surface that extends to the toe of the slope. Due to the consideration of strain softening, the material properties in the vicinity of the thermal-induced shear zone deteriorate further, leading to a global slipping, while soil within the sliding block is observed to exhibit little failure. It is noteworthy that during the early stage of the shear band formation, the pore pressure decreases within the shear band while it increases outside the shear band. However, with the continued slide progression, the pore pressure of the internal soil near the fixed end

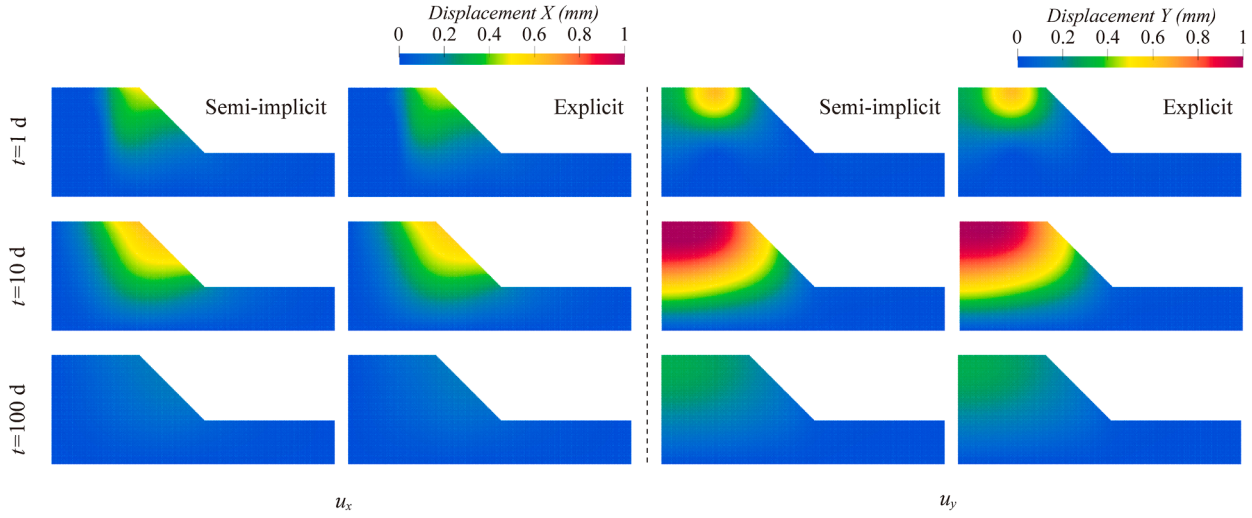


**Fig. 21.** Lateral and vertical displacement at different time instances during the heating process for both the semi-implicit and explicit MPM.

begins to dissipate also, potentially due to the suction effect of the shear band and geometric changes after slope failure. The contour figures demonstrate that the simulation outcomes are both reasonable and stable, highlighting the potential success of the proposed method in the analysis of thermo-hydro-mechanically coupled large deformation problems.

**Remarks**. This example illustrates the proposed framework's capability to simulate the THM response of a slope during heating and the thermal-induced slope failure, indicating its adaptability to a wide range of problems, from small to large deformation regimes. The proposed method is also suitable for simulating the entire failure process of complex multiphysics coupling scenarios, from initiation and propagation to post-failure stages, which can be challenging for FEM. While the study focuses on the numerical aspects of the framework, it is noteworthy that the plastic dissipation term, representing mechanical plastic work converted into heat, is not

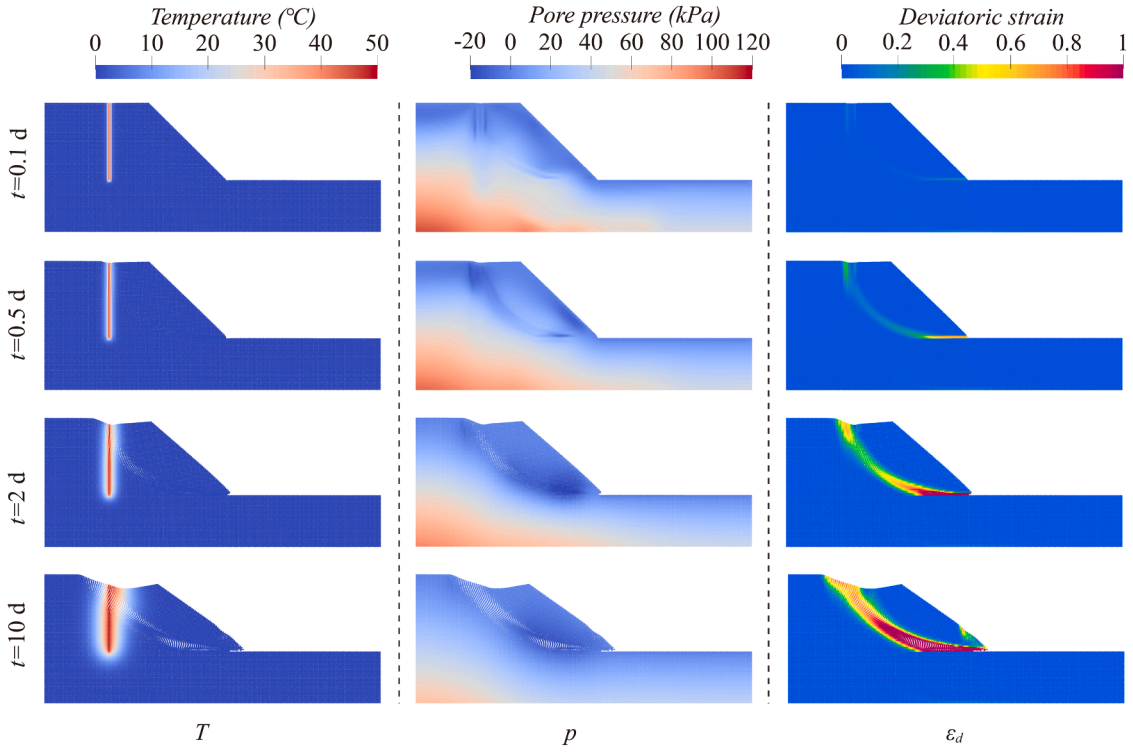


**Fig. 22.** Contours of temperature, pore pressure, and deviatoric strain for semi-implicit MPM at $t = 0.1$ d, 0.5 d, 2 d, and 10 d.

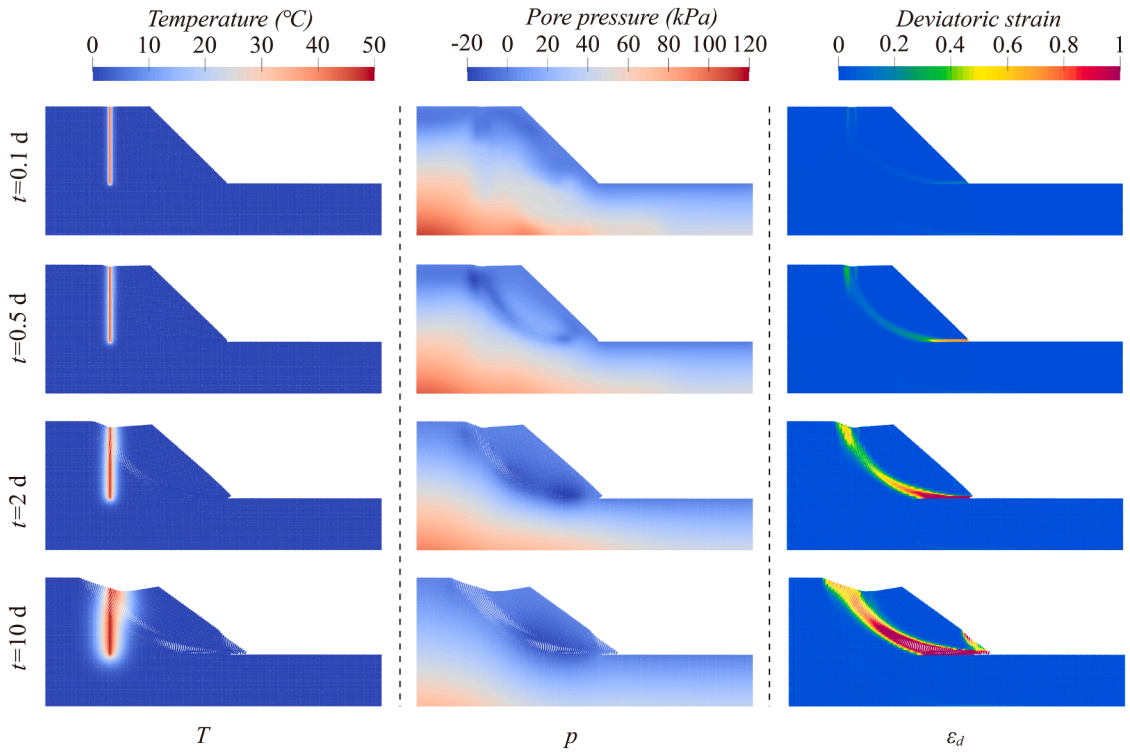


**Fig. 23.** Contours of temperature, pore pressure, and deviatoric strain for explicit MPM at $t = 0.1$ d, 0.5 d, 2 d, and 10 d.

considered in this example. Several studies have emphasized the significant impact of plastic dissipation on hydraulic and mechanical responses, indicating the need for its inclusion [8,66,67]. For instance, Seguí et al. [67] found that the movement of landslide causes friction in the shear band, raising the temperature of the clays until they become unstable and collapse catastrophically through a thermal runaway instability. It is also found that the nonlinear plasticity coupling term in the heat equation may introduce additional numerical instabilities and errors, requiring special treatment, especially when the sequential solution scheme is adopted [68,69]. The monolithic scheme is likely an effective way to improve the numerical accuracy when dealing with complex tightly coupled THM systems [18,46,94]. However, it remains challenging for THM-coupled MPM to ensure convergency and stability in the context of large deformation regimes. Additionally, the constitutive model used in this example is relatively simplistic, which may limit the fidelity of the simulation. Therefore, future research will consider investigating different solution schemes and alternative stress–strain updating techniques.

## 6. Conclusions

A THM-coupled material point method (MPM) has been developed for simulating large deformation problems in saturated porous media. The fully coupled governing equations are derived within the framework of one-point, two-phase MPM via ***u-v-p-T*** formulation. A simple and efficient staggered time integration scheme is proposed, in which the energy balance equation is solved explicitly, and the hydrodynamic part is solved based on the fractional step method. Both cases of compressible and weakly compressible fluid are considered. A fully explicit scheme for the coupled equations is also developed for comparison purposes. To facilitate the simulation of 3D axisymmetric THM problems, the axisymmetric formulations are also derived after necessary modifications from the plane strain formulation.

The proposed THM-coupled MPM has been validated using two well-documented examples, including the heating problem of saturated half-space, which was analytically solved by McTigue [76], and the non-isothermal consolidation problem of a saturated soil column, which is well-benchmarked by many finite element analyses. Numerical results show that the particle temperatures updated based on incremental nodal temperatures are accurate, whereas the method by directly extrapolating nodal temperatures encounters unacceptable errors caused by numerical heat transfer. By employing the fractional time step, the issue of pore pressure oscillation can be effectively resolved. The explicit method is found prone to pressure oscillations even after using the pressure smoothing technique. The proposed axisymmetric formulation is further verified based on a 3D axisymmetric case, namely, the thermoelastic response problem around a deeply buried heat source.

The performance of the proposed method in modeling large deformation problems has further been demonstrated by predicting the progressive failure of a saturated slope in which the soil properties (i.e., cohesion and frictional angle) are sensitive to temperature changes. This case highlights the significant potential of the coupled MPM in simulating the THM-involved large deformation process

in regions containing thermally or mechanically sensitive soils, such as the submarine landslides or borehole breakout caused by methane hydrate exploitation and the thawing subsidence or collapse of permafrost caused by global warming. However, it is important to note that these engineering problems involve important phase transition processes that are not considered in the current method. The strong nonlinearity and tight coupling in such complex multiphase, multicomponent, and multiphysics porous systems may require more advanced MPM solvers, such as a high-efficiency stabilized monolithic solver, to improve the accuracy of the simulation results. Furthermore, the complexity of such granular materials necessitates the development of advanced constitutive models or alternative tools, such as the multiscale method as documented by the authors [37,41,95–98]. These scientific challenges will be addressed in future studies.

## Declaration of competing interest

The authors declare that they have no known competing financial interests or personal relationships that could have appeared to influence the work reported in this paper.

## Data availability

Data will be made available on request.

## Acknowledgments

This work is financially supported by National Natural Science Foundation of China (via Project #11972030), Research Grants Council of Hong Kong (GRF #16208720, CRF #C7082-22G, F-HKUST601/19), and Science and Technology Program of Guangzhou (202201010392). The authors appreciate the constructive comments made by both anonymous reviewers.

## Appendix. Axisymmetric formulations

To facilitate modeling axisymmetric conditions that are often encountered in thermal coupled geological problems, such as engineering processes involving point heat source, thermal pile, and wellbore, we also provide the axisymmetric form of THM-coupled MPM by modifying from the 2D plane strain formulations. Indeed, Sulsky and Schreyer [99] suggested that it is possible to directly use the planar shape functions for the axisymmetric problem in standard MPM. Nairn and Guilkey [39] further extended the formulation to GIMP by modifying the shape functions. Compared with Cartesian formulations, the key changes are to replace the volume integration by cylindrical volume integration and to account for cylindrical coordinates in gradient evaluations.

### *A.1. Particle volume*

In axisymmetric MPM, the position of a material point $p$ is characterized by $(r_p, z_p)$, where $r_p$ and $z_p$ are the radial and the axial positions, respectively, interchangeable with $x_p$ and $z_p$ in Cartesian coordinate, and the third dimension, angular coordinate $\theta_p$, is taken as 1 radian. The subdomain of a material point in axisymmetric MPM is no longer a plane but a one-radian wedge, and its volume is calculated by,

$$V_p = \int_{\Omega_p} \chi_p(r,z) r \mathrm{d}r\mathrm{d}z = A_p \bar{r}_p \tag{50}$$

where $A_p$ is the area of particle $p$, and $\bar{r}_p$ is the radial position of particle $p$.

### *A.2. Shape functions*

For GIMP, the shape functions are calculated as follows,

$$S_{ip} = \frac{1}{A_p \bar{r}_p} \int_\Omega \chi_p(r,z) N_i(r,z) r \mathrm{d}r\mathrm{d}z \tag{51a}$$

$$\nabla S_{ip} = \frac{1}{A_p \bar{r}_p} \int_\Omega \chi_p(r,z) \nabla N_i(r,z) r \mathrm{d}r\mathrm{d}z \tag{51b}$$

$$T_{ip} = \frac{1}{A_p \bar{r}_p} \int_\Omega \chi_p(r,z) N_i(r,z) \mathrm{d}r\mathrm{d}z \tag{51c}$$

An extra shape function $T_{ip}$ is needed for axisymmetric MPM. By selecting $\chi_p(r,z) = A_p \delta(r_p, z_p)$, it results in $S_{ip} = N_{ip}$, $\nabla S_{ip} = \nabla N_{ip}$, and

$T_{ip} = N_{ip}/r_p$ for standard MPM.

### A.3. Particle strains

By evaluating the velocity gradient in cylindrical coordinate, one can obtain the strain increment $\Delta\boldsymbol{\varepsilon}_{sp}^{k}$ with each non-zero component given as,

$$\left(\Delta\varepsilon_{sp}^{k+1}\right)_{rr} = \sum_i \left(\Delta v_{si}^{k+1}\right)_r \left(\nabla S_{ip}\right)_r \tag{52a}$$

$$\left(\Delta\varepsilon_{sp}^{k+1}\right)_{zz} = \sum_i \left(\Delta v_{si}^{k}\right)_z \left(\nabla S_{ip}\right)_z \tag{52b}$$

$$\left(\Delta\varepsilon_{sp}^{k+1}\right)_{rz} = \frac{1}{2}\sum_i \left(\left(\Delta v_{si}^{k}\right)_z \left(\nabla S_{ip}\right)_r + \left(\Delta v_{si}^{k}\right)_r \left(\nabla S_{ip}\right)_z\right) \tag{52c}$$

$$\left(\Delta\varepsilon_{sp}^{k+1}\right)_{\theta\theta} = \sum_i \left(\Delta v_{si}^{k}\right)_r T_{ip} \tag{52d}$$

where $\left(\Delta v_{si}^{k}\right)_r$ and $\left(\Delta v_{si}^{k}\right)_z$ are the radial and axial components of nodal velocity $\boldsymbol{v}_{si}^{k}$, and $\left(\nabla S_{ip}\right)_r$ and $\left(\nabla S_{ip}\right)_z$ are the radial and axial components of $\nabla S_{ip}$. The difference is the deformation has a hoop direction strain $\left(\Delta\varepsilon_{sp}^{k}\right)_{\theta\theta}$ compared with the plane strain problem.

### A.4. Nodal internal forces

By evaluating the stress gradient, the internal force can be reformulated with components in each dimension calculated by,

$$\left(\mathscr{F}_{\alpha}^{int}\right)_r = -\sum_p V_p \left[\left(\sigma_{ap}^{k}\right)_{rr} \left(\nabla \boldsymbol{S}_p\right)_r + \left(\sigma_{ap}^{k}\right)_{rz} \left(\nabla \boldsymbol{S}_p\right)_z + \left(\sigma_{ap}^{k}\right)_{\theta\theta} \boldsymbol{T}_p\right] \tag{53a}$$

$$\left(\mathscr{F}_{\alpha}^{int}\right)_z = -\sum_p V_p \left[\left(\sigma_{ap}^{k}\right)_{rz} \left(\nabla \boldsymbol{S}_p\right)_r + \left(\sigma_{ap}^{k}\right)_{zz} \left(\nabla \boldsymbol{S}_p\right)_z\right] \tag{53b}$$

where $\left(\sigma_{ap}^{k}\right)_{\theta\theta}$ is the hoop stress. Note that $r$ in cylindrical coordinates is interchangeable with $x$ in Cartesian coordinates, so the only change is the consideration of the hoop stress term. Similarly, the corrected internal force should also be modified by evaluating $\mathscr{F}_{\alpha}^{cor}$ with each component calculated by,

$$\left(\mathscr{F}_{\alpha}^{cor}\right)_r = -\sum_p \boldsymbol{S}_p^T V_{ap} \left[\left(\nabla \boldsymbol{S}_p\right)_r + \left(\nabla \boldsymbol{S}_p\right)_z + \boldsymbol{T}_p\right] \tag{54a}$$

$$\left(\mathscr{F}_{\alpha}^{cor}\right)_z = -\sum_p \boldsymbol{S}_p^T V_{ap} \left[\left(\nabla \boldsymbol{S}_p\right)_r + \left(\nabla \boldsymbol{S}_p\right)_z\right] \tag{54b}$$

Apart from the above modifications, the boundary conditions, such as the heat source and the traction force, should also be correctly prescribed based on the particle or node positions.

## References

[1] M.M. Tamizdoust, O. Ghasemi-Fare, A fully coupled thermo-poro-mechanical finite element analysis to predict the thermal pressurization and thermally induced pore fluid flow in soil media, Comput. Geotech. 117 (2020), 103250, https://doi.org/10.1016/j.compgeo.2019.103250.

[2] W.F. Waite, J.C. Santamarina, D.D. Cortes, B. Dugan, D.N. Espinoza, J. Germaine, J. Jang, J.W. Jung, T.J. Kneafsey, H. Shin, K. Soga, W.J. Winters, T.-S. Yun, Physical properties of hydrate-bearing sediments, Rev. Geophys. 47 (2009), https://doi.org/10.1029/2008RG000279.

[3] C.F. Tsang, J.D. Barnichon, J. Birkholzer, X.L. Li, H.H. Liu, X. Sillen, Coupled thermo-hydro-mechanical processes in the near field of a high-level radioactive waste repository in clay formations, Int. J. Rock Mech. Min. Sci. 49 (2012) 31–44, https://doi.org/10.1016/j.ijrmms.2011.09.015.
[4] T.T. Garipov, M.H. Hui, Discrete fracture modeling approach for simulating coupled thermo-hydro-mechanical effects in fractured reservoirs, Int. J. Rock Mech. Min. Sci. 122 (2019), 104075, https://doi.org/10.1016/j.ijrmms.2019.104075.
[5] I. Vardoulakis, Dynamic thermo-poro-mechanical analysis of catastrophic landslides, Géotechnique 52 (2002) 157–171, https://doi.org/10.1680/geot.2002.52.3.157.
[6] E. Veveakis, I. Vardoulakis, G. Di Toro, Thermoporomechanics of creeping landslides: The 1963 vaiont slide, northern Italy, J. Geophys. Res.: Earth Surf. 112 (2007), https://doi.org/10.1029/2006JF000702.
[7] K. Yamamoto, T. Kanno, X.-X. Wang, M. Tamaki, T. Fujii, S.-S. Chee, X.-W. Wang, V. Pimenov, V. Shako, Thermal responses of a gas hydrate-bearing sediment to a depressurization operation, RSC Adv. 7 (2017) 5554–5577, https://doi.org/10.1039/C6RA26487E.
[8] N.M. Pinyol, M. Alvarado, E.E. Alonso, F. Zabala, Thermal effects in landslide mobility, Géotechnique 68 (2018) 528–545, https://doi.org/10.1680/jgeot.17.P.054.
[9] E.E. Alonso, Triggering and motion of landslides, Géotechnique 71 (2021) 3–59, https://doi.org/10.1680/jgeot.20.RL.001.
[10] J. Noorishad, C.F. Tsang, P.A. Witherspoon, Coupled thermal-hydraulic-mechanical phenomena in saturated fractured porous rocks: Numerical approach, J. Geophys. Res. 89 (1984) 10365–10373, https://doi.org/10.1029/JB089iB12p10365.
[11] R.W. Lewis, C.E. Majorana, B.A. Schrefler, A coupled finite element model for the consolidation of nonisothermal elastoplastic porous media, Transp. Porous. Med. 1 (1986) 155–178, https://doi.org/10.1007/BF00714690.
[12] D. Gawin, B.A. Schrefler, M. Galindo, Thermo-hydro-mechanical analysis of partially saturated porous materials, Eng. Comput. 13 (1996) 113–143, https://doi.org/10.1108/02644409610151584.
[13] X. Li, Z. Liu, R.W. Lewis, Mixed finite element method for coupled thermo-hydro-mechanical process in poro-elasto-plastic media at large strains, Internat. J. Numer. Methods Engrg. 64 (2005) 667–708, https://doi.org/10.1002/nme.1469.
[14] F. Tong, L. Jing, R.W. Zimmerman, A fully coupled thermo-hydro-mechanical model for simulating multiphase flow, deformation and heat transfer in buffer material and rock masses, Int. J. Rock Mech. Min. Sci. 47 (2010) 205–217, https://doi.org/10.1016/j.ijrmms.2009.11.002.
[15] T.D. Cao, L. Sanavia, B.A. Schrefler, A thermo-hydro-mechanical model for multiphase geomaterials in dynamics with application to strain localization simulation, Internat. J. Numer. Methods Engrg. 107 (2016) 312–337, https://doi.org/10.1002/nme.5175.
[16] S. Li, X. Li, D. Zhang, A fully coupled thermo-hydro-mechanical, three-dimensional model for hydraulic stimulation treatments, J. Nat. Gas Sci. Eng. 34 (2016) 64–84, https://doi.org/10.1016/j.jngse.2016.06.046.
[17] W. Cui, D.M. Potts, L. Zdravković, K.A. Gawecka, D.M.G. Taborda, An alternative coupled thermo-hydro-mechanical finite element formulation for fully saturated soils, Comput. Geotech. 94 (2018) 22–30, https://doi.org/10.1016/j.compgeo.2017.08.011.
[18] X. Cui, L.N.Y. Wong, A 3D fully thermo–hydro–mechanical coupling model for saturated poroelastic medium, Comput. Methods Appl. Mech. Engrg. 394 (2022), 114939, https://doi.org/10.1016/j.cma.2022.114939.
[19] S.r. Idelsohn, E. Oñate, F.D. Pin, The particle finite element method: a powerful tool to solve incompressible flows with free-surfaces and breaking waves, Internat. J. Numer. Methods Engrg. 61 (2004) 964–989, https://doi.org/10.1002/nme.1096.
[20] S.G. Bardenhagen, J.U. Brackbill, D. Sulsky, The material-point method for granular materials, Comput. Methods Appl. Mech. Engrg. 187 (2000) 529–541, https://doi.org/10.1016/S0045-7825(99)00338-2.
[21] D. Sulsky, S.J. Zhou, H.L. Schreyer, Application of a particle-in-cell method to solid mechanics, Comput. Phys. Commun. Particle Simul. Methods 87 (1995) 236–252, https://doi.org/10.1016/0010-4655(94)00170-7.
[22] A. Stomakhin, C. Schroeder, C. Jiang, L. Chai, J. Teran, A. Selle, Augmented MPM for phase-change and varied materials, ACM Trans. Graph. 33 (138:1-138:11) (2014), https://doi.org/10.1145/2601097.2601176.
[23] Y. Liang, X. Zhang, Y. Liu, An efficient staggered grid material point method, Comput. Methods Appl. Mech. Engrg. 352 (2019) 85–109, https://doi.org/10.1016/j.cma.2019.04.024.
[24] H. Su, T. Xue, C. Han, C. Jiang, M. Aanjaneya, A unified second-order accurate in time MPM formulation for simulating viscoelastic liquids with phase change, ACM Trans. Graph. 40 (2021) 119:1–119:18, https://doi.org/10.1145/3450626.3459820.
[25] H.W. Zhang, K.P. Wang, Z. Chen, Material point method for dynamic analysis of saturated porous media under external contact/impact of solid bodies, Comput. Methods Appl. Mech. Engrg. 198 (2009) 1456–1472, https://doi.org/10.1016/j.cma.2008.12.006.
[26] I. Jassim, D. Stolle, P. Vermeer, Two-phase dynamic analysis by material point method, Int. J. Numer. Anal. Methods Geomech. 37 (2013) 2502–2522, https://doi.org/10.1002/nag.2146.
[27] A. Yerro, E.E. Alonso, N.M. Pinyol, Run-out of landslides in brittle soils, Comput. Geotech. 80 (2016) 427–439, https://doi.org/10.1016/j.compgeo.2016.03.001.
[28] S. Bandara, K. Soga, Coupling of soil deformation and pore fluid flow using material point method, Comput. Geotech. 63 (2015) 199–214, https://doi.org/10.1016/j.compgeo.2014.09.009.
[29] F. Ceccato, L. Beuth, P.A. Vermeer, P. Simonini, Two-phase material point method applied to the study of cone penetration, Comput. Geotech. 80 (2016) 440–452, https://doi.org/10.1016/j.compgeo.2016.03.003.
[30] Z.-P. Chen, X. Zhang, K.Y. Sze, L. Kan, X.-M. Qiu, V-p material point method for weakly compressible problems, Comput. & Fluids 176 (2018) 170–181, https://doi.org/10.1016/j.compfluid.2018.09.005.
[31] Y. Zhao, J. Choo, Stabilized material point methods for coupled large deformation and fluid flow in porous materials, Comput. Methods Appl. Mech. Engrg. 362 (2020), 112742, https://doi.org/10.1016/j.cma.2019.112742.
[32] X. Lei, S. He, X. Chen, H. Wong, L. Wu, E. Liu, A generalized interpolation material point method for modelling coupled seepage-erosion-deformation process within unsaturated soils, Adv. Water Resour. 141 (2020), 103578, https://doi.org/10.1016/j.advwatres.2020.103578.
[33] S. Kularathna, W. Liang, T. Zhao, B. Chandra, J. Zhao, K. Soga, A semi-implicit material point method based on fractional-step method for saturated soil, Int. J. Numer. Anal. Methods Geomech. 45 (2021) 1405–1436, https://doi.org/10.1002/nag.3207.
[34] K. Feng, G. Wang, D. Huang, F. Jin, Material point method for large-deformation modeling of coseismic landslide and liquefaction-induced dam failure, Soil Dyn. Earthq. Eng. 150 (2021), 106907, https://doi.org/10.1016/j.soildyn.2021.106907.
[35] X. Zheng, F. Pisanò, P.J. Vardon, M.A. Hicks, An explicit stabilised material point method for coupled hydromechanical problems in two-phase porous media, Comput. Geotech. 135 (2021), 104112, https://doi.org/10.1016/j.compgeo.2021.104112.
[36] X. Zheng, F. Pisanò, P.J. Vardon, M.A. Hicks, Fully implicit, stabilised MPM simulation of large-deformation problems in two-phase elastoplastic geomaterials, Comput. Geotech. 147 (2022), 104771, https://doi.org/10.1016/j.compgeo.2022.104771.
[37] W. Liang, J. Zhao, H. Wu, K. Soga, Multiscale, multiphysics modeling of saturated granular materials in large deformation, Comput. Methods Appl. Mech. Engrg. 405 (2023), 115871, https://doi.org/10.1016/j.cma.2022.115871.
[38] K. Soga, E. Alonso, A. Yerro, K. Kumar, S. Bandara, Trends in large-deformation analysis of landslide mass movements with particular emphasis on the material point method, Géotechnique 66 (2016) 248–273, https://doi.org/10.1680/jgeot.15.LM.005.
[39] J.A. Nairn, J.E. Guilkey, Axisymmetric form of the generalized interpolation material point method, Internat. J. Numer. Methods Engrg. 101 (2015) 127–147, https://doi.org/10.1002/nme.4792.
[40] J. Tao, H. Zhang, Y. Zheng, Z. Chen, Development of generalized interpolation material point method for simulating fully coupled thermomechanical failure evolution, Comput. Methods Appl. Mech. Engrg. 332 (2018) 325–342, https://doi.org/10.1016/j.cma.2017.12.014.
[41] S. Zhao, J. Zhao, W. Liang, F. Niu, Multiscale modeling of coupled thermo-mechanical behavior of granular media in large deformation and flow, Comput. Geotech. 149 (2022), 104855, https://doi.org/10.1016/j.compgeo.2022.104855.
[42] X. Lei, S. He, A. Abed, X. Chen, Z. Yang, Y. Wu, A generalized interpolation material point method for modelling coupled thermo-hydro-mechanical problems, Comput. Methods Appl. Mech. Engrg. 386 (2021), 114080, https://doi.org/10.1016/j.cma.2021.114080.

[43] O.C. Zienkiewicz, C.T. Chang, P. Bettess, Drained, undrained, consolidating and dynamic behaviour assumptions in soils, Géotechnique 30 (1980) 385–395, https://doi.org/10.1680/geot.1980.30.4.385.
[44] W.-H. Yuan, J.-X. Zhu, K. Liu, W. Zhang, B.-B. Dai, Y. Wang, Dynamic analysis of large deformation problems in saturated porous media by smoothed particle finite element method, Comput. Methods Appl. Mech. Engrg. 392 (2022), 114724, https://doi.org/10.1016/j.cma.2022.114724.
[45] V. Kazemi-Kamyab, A.H. van Zuijlen, H. Bijl, A high order time-accurate loosely-coupled solution algorithm for unsteady conjugate heat transfer problems, Comput. Methods Appl. Mech. Engrg. 264 (2013) 205–217, https://doi.org/10.1016/j.cma.2013.05.021.
[46] B. Gee, R. Gracie, Comparison of fully-coupled and sequential solution methodologies for enhanced geothermal systems, Comput. Methods Appl. Mech. Engrg. 373 (2021), 113554, https://doi.org/10.1016/j.cma.2020.113554.
[47] K.J. Bathe, The inf–sup condition and its evaluation for mixed finite element methods, Comput. Struct. 79 (2) (2001) 243–252.
[48] J.A. White, R.I. Borja, Stabilized low-order finite elements for coupled solid-deformation/fluid-diffusion and their application to fault zone transients, Comput. Methods Appl. Mech. Engrg. 197 (2008) 4353–4366, https://doi.org/10.1016/j.cma.2008.05.015.
[49] J.B. Haga, H. Osnes, H.P. Langtangen, On the causes of pressure oscillations in low-permeable and low-compressible porous media, Int. J. Numer. Anal. Methods Geomech. 36 (2012) 1507–1522, https://doi.org/10.1002/nag.1062.
[50] L. Monforte, P. Navas, J.M. Carbonell, M. Arroyo, A. Gens, Low-order stabilized finite element for the full Biot formulation in soil mechanics at finite strain, Int. J. Numer. Anal. Methods Geomech. 43 (2019) 1488–1515, https://doi.org/10.1002/nag.2923.
[51] W.-H. Yuan, M. Liu, X.-W. Zhang, H.-L. Wang, W. Zhang, W. Wu, Stabilized smoothed particle finite element method for coupled large deformation problems in geotechnics, Acta Geotech. (2022), https://doi.org/10.1007/s11440-022-01691-6.
[52] Y. Zhang, D. Pedroso, L. Li, FDM and FEM solutions to linear dynamics of porous media: stabilised, monolithic and fractional schemes, Internat. J. Numer. Methods Engrg. 108 (2016) n/a–n/a, https://doi.org/10.1002/nme.5231.
[53] R. Codina, J. Blasco, A finite element formulation for the Stokes problem allowing equal velocity-pressure interpolation, Comput. Methods Appl. Mech. Engrg. 143 (1997) 373–391, https://doi.org/10.1016/S0045-7825(96)01154-1.
[54] R. Codina, J. Blasco, Analysis of a pressure-stabilized finite element approximation of the stationary Navier–Stokes equations, Numer. Math. 87 (2000) 59–81, https://doi.org/10.1007/s002110000174.
[55] R. Codina, S. Badia, On some pressure segregation methods of fractional-step type for the finite element approximation of incompressible flow problems, Comput. Methods Appl. Mech. Eng. Incompress. CFD 195 (2006) 2900–2918, https://doi.org/10.1016/j.cma.2004.06.048.
[56] R. Codina, Pressure stability in fractional step finite element methods for incompressible flows, J. Comput. Phys. 170 (2001) 112–140, https://doi.org/10.1006/jcph.2001.6725.
[57] S. Badia, R. Codina, Convergence analysis of the FEM approximation of the first order projection method for incompressible flows with and without the inf-sup condition, Numer. Math. 107 (2007) 533–557, https://doi.org/10.1007/s00211-007-0099-5.
[58] B. Markert, Y. Heider, W. Ehlers, Comparison of monolithic and splitting solution schemes for dynamic porous media problems, Internat. J. Numer. Methods Engrg. 82 (2010) 1341–1383, https://doi.org/10.1002/nme.2789.
[59] Y. Jia, Y. Wileveau, K. Su, G. Duveau, J.F. Shao, Thermo-hydro-mechanical modelling of an in situ heating experiment, Géotechnique 57 (2007) 845–855, https://doi.org/10.1680/geot.2007.57.10.845.
[60] A.P.S. Selvadurai, M. Najari, The thermo-hydro-mechanical behavior of the argillaceous cobourg limestone, J. Geophys. Res.: Solid Earth 122 (2017) 4157–4171, https://doi.org/10.1002/2016JB013744.
[61] Z. Michalec, R. Blaheta, M. Hasal, T. Ligurský, Fully coupled thermo-hydro-mechanical model with oversaturation and its validation to experimental data from FEBEX experiment, Int. J. Rock Mech. Min. Sci. 139 (2021), 104567, https://doi.org/10.1016/j.ijrmms.2020.104567.
[62] R.M. Bowen, Incompressible porous media models by use of the theory of mixtures, Internat. J. Engrg. Sci. 18 (1980) 1129–1148, https://doi.org/10.1016/0020-7225(80)90114-7.
[63] R.M. Bowen, Compressible porous media models by use of the theory of mixtures, Internat. J. Engrg. Sci. 20 (1982) 697–735, https://doi.org/10.1016/0020-7225(82)90082-9.
[64] R.W. Lewis, R.W. Lewis, B.A. Schrefler, The Finite Element Method in the Static and Dynamic Deformation and Consolidation of Porous Media, John Wiley & Sons, 1998.
[65] D.M. Pedroso, A consistent u-p formulation for porous media with hysteresis, Internat. J. Numer. Methods Engrg. 101 (2015) 606–634, https://doi.org/10.1002/nme.4808.
[66] T. Poulet, M. Paesold, M. Veveakis, Multi-physics modelling of fault mechanics using REDBACK: A parallel open-source simulator for tightly coupled problems, Rock Mech. Rock Eng. 50 (2017) 733–749, https://doi.org/10.1007/s00603-016-0927-y.
[67] C. Seguí, H. Rattez, M. Veveakis, On the stability of deep-seated landslides. The cases of vaiont (Italy) and shuping (three gorges dam, China), J. Geophys. Res.: Earth Surf. 125 (2020), e2019JF005203, https://doi.org/10.1029/2019JF005203.
[68] T. Poulet, M. Veveakis, A viscoplastic approach for pore collapse in saturated soft rocks using REDBACK: An open-source parallel simulator for rock mechanics with dissipative feedbacks, Comput. Geotech. 74 (2016) 211–221, https://doi.org/10.1016/j.compgeo.2015.12.015.
[69] M. Sari, S. Alevizos, T. Poulet, J. Lin, M. Veveakis, A visco-plastic framework for interface processes in sedimentary reservoir rocks at HPHT conditions, Geomech. Energy Environ. 22 (2020), 100165, https://doi.org/10.1016/j.gete.2019.100165.
[70] M.m.j. Mieremet, D.f. Stolle, F. Ceccato, C. Vuik, Numerical stability for modelling of dynamic two-phase interaction, Int. J. Numer. Anal. Methods Geomech. 40 (2016) 1284–1294, https://doi.org/10.1002/nag.2483.
[71] J.L. Guermond, P. Minev, J. Shen, An overview of projection methods for incompressible flows, Comput. Methods Appl. Mech. Engrg. 195 (2006) 6011–6045, https://doi.org/10.1016/j.cma.2005.10.010.
[72] S.M. Hosseini, J.J. Feng, Pressure boundary conditions for computing incompressible flows with SPH, J. Comput. Phys. 230 (2011) 7473–7487, https://doi.org/10.1016/j.jcp.2011.06.013.
[73] S.G. Bardenhagen, E.M. Kober, The generalized interpolation material point method, Comput. Model. Eng. Sci. 5 (6) (2004) 477–496, https://doi.org/10.3970/cmes.2004.005.477.
[74] K. Kumar, J. Salmond, S. Kularathna, C. Wilkes, E. Tjung, G. Biscontin, K. Soga, Scalable and modular material point method for large scale simulations, in: 2nd International Conference on the Material Point Method, Cambridge, UK, 2019, https://arxiv.org/abs/1909.13380.
[75] C.C. Hammerquist, J.A. Nairn, A new method for material point method particle updates that reduces noise and enhances stability, Comput. Methods Appl. Mech. Engrg. 318 (2017) 724–738, https://doi.org/10.1016/j.cma.2017.01.035.
[76] D.F. McTigue, Thermoelastic response of fluid-saturated porous rock, J. Geophys. Res. 91 (9533) (1986), https://doi.org/10.1029/JB091iB09p09533.
[77] B.L. Aboustit, S.H. Advani, J.K. Lee, R.S. Sandhu, Finite element evaluations of thermo-elastic consolidation, in: Presented At the the 23rd U.S Symposium on Rock Mechanics (USRMS), OnePetro., 1982.
[78] B.L. Aboustit, S.H. Advani, J.K. Lee, Variational principles and finite element simulations for thermo-elastic consolidation, Int. J. Numer. Anal. Methods Geomech. 9 (1985) 49–69, https://doi.org/10.1002/nag.1610090105.
[79] L.-J. Wang, B. Zhu, Y.-M. Chen, R.-P. Chen, X.S. Shi, Precise model for predicting excess pore-water pressure of layered soils induced by thermal-mechanical loads, J. Eng. Mech. 145 (2019), 04018114, https://doi.org/10.1061/(ASCE)EM.1943-7889.0001544.
[80] B. Bai, Thermal consolidation of layered porous half-space to variable thermal loading, Appl. Math. Mech. 27 (2006) 1531–1539, https://doi.org/10.1007/s10483-006-1111-1.
[81] B. Bai, Fluctuation responses of saturated porous media subjected to cyclic thermal loading, Comput. Geotech. 33 (2006) 396–403, https://doi.org/10.1016/j.compgeo.2006.08.005.
[82] J.R. Booker, C. Savvidou, Consolidation around a point heat source, Int. J. Numer. Anal. Methods Geomech. 9 (1985) 173–184, https://doi.org/10.1002/nag.1610090206.

[83] A.A. Chaudhry, J. Buchwald, O. Kolditz, T. Nagel, Consolidation around a point heat source (correction and verification), Int. J. Numer. Anal. Methods Geomech. 43 (2019) 2743–2751, https://doi.org/10.1002/nag.2998.
[84] W.M. Coombs, T.J. Charlton, M. Cortis, C.E. Augarde, Overcoming volumetric locking in material point methods, Comput. Methods Appl. Mech. Engrg. 333 (2018) 1–21, https://doi.org/10.1016/j.cma.2018.01.010.
[85] S. Na, W. Sun, Computational thermo-hydro-mechanics for multiphase freezing and thawing porous media in the finite deformation range, Comput. Methods Appl. Mech. Engrg. 318 (2017) 667–700, https://doi.org/10.1016/j.cma.2017.01.028.
[86] S. Nishimura, A. Gens, S. Olivella, R.J. Jardine, THM-coupled finite element analysis of frozen soil: formulation and application, Géotechnique 59 (2009) 159–171, https://doi.org/10.1680/geot.2009.59.3.159.
[87] Y. Lu, S. Liu, E. Alonso, L. Wang, L. Xu, Z. Li, Volume changes and mechanical degradation of a compacted expansive soil under freeze-thaw cycles, Cold Reg. Sci. & Technol. 157 (2019) 206–214, https://doi.org/10.1016/j.coldregions.2018.10.008.
[88] S. Zhao, H. Chen, J. Zhao, Multiscale modeling of freeze-thaw behavior in granular media, Acta Mech. Sinica 39 (2023), 722195, https://doi.org/10.1007/s10409-022-22195-x.
[89] X. Ma, Y. Sun, B. Liu, W. Guo, R. Jia, B. Li, S. Li, Numerical study of depressurization and hot water injection for gas hydrate production in China's first offshore test site, J. Nat. Gas Sci. Eng. 83 (2020), 103530, https://doi.org/10.1016/j.jngse.2020.103530.
[90] D. Wang, W. Ma, Y. Niu, X. Chang, Z. Wen, Effects of cyclic freezing and thawing on mechanical properties of qinghai–tibet clay, Cold Reg. Sci. & Technol. 48 (2007) 34–43, https://doi.org/10.1016/j.coldregions.2006.09.008.
[91] P. Monterey, K.J. Willam, Triaxial failure criterion for concrete and its generalization, Struct. J. 92 (3) (1995) 311–318.
[92] H. Chen, S. Zhao, J. Zhao, X. Zhou, DEM-enriched contact approach for material point method, Comput. Methods Appl. Mech. Engrg. 404 (2023), 115814, https://doi.org/10.1016/j.cma.2022.115814.
[93] Y. Lian, H.H. Bui, G.D. Nguyen, S. Zhao, A. Haque, A computationally efficient SPH framework for unsaturated soils and its application to predicting the entire rainfall-induced slope failure process, Géotechnique (2022) 1–19, https://doi.org/10.1680/jgeot.21.00349.
[94] M. Lesueur, M.C. Casadiego, M. Veveakis, T. Poulet, Modelling fluid-microstructure interaction on elasto-visco-plastic digital rocks, Geomech. Energy Environ. 12 (2017) 1–13, https://doi.org/10.1016/j.gete.2017.08.001.
[95] N. Guo, J. Zhao, Parallel hierarchical multiscale modelling of hydro-mechanical problems for saturated granular soils, Comput. Methods Appl. Mech. Engrg. 305 (2016) 37–61, https://doi.org/10.1016/j.cma.2016.03.004.
[96] W. Liang, J. Zhao, Multiscale modeling of large deformation in geomechanics, Int. J. Numer. Anal. Methods Geomech. 43 (2019) 1080–1114, https://doi.org/10.1002/nag.2921.
[97] W. Liang, S. Zhao, H. Wu, J. Zhao, Bearing capacity and failure of footing on anisotropic soil: A multiscale perspective, Comput. Geotech. 137 (2021), 104279, https://doi.org/10.1016/j.compgeo.2021.104279.
[98] S. Zhao, J. Zhao, Y. Lai, Multiscale modeling of thermo-mechanical responses of granular materials: A hierarchical continuum–discrete coupling approach, Comput. Methods Appl. Mech. Engrg. 367 (2020), 113100, https://doi.org/10.1016/j.cma.2020.113100.
[99] D. Sulsky, H.L. Schreyer, Axisymmetric form of the material point method with applications to upsetting and taylor impact problems, Comput. Methods Appl. Mech. Engrg. 139 (1996) 409–429, https://doi.org/10.1016/S0045-7825(96)01091-2.